nature chemical biology

Article

https://doi.org/10.1038/s41589-023-01364-9

Nanosensor-based monitoring of autophagy-associated lysosomal acidification in vivo

Received: 5 August 2022

Accepted: 12 May 2023

Mijin Kim[1,7], **Chen Chen**[1,2,3,7], **Zvi Yaari**[1,6], **Rune Frederiksen**[1], **Ewelina Randall**[1], **Jaina Wollowitz**[1,2,3], **Christian Cupo**[1], **Xiaojian Wu**[4], **Janki Shah**[1], **Daniel Worroll**[1], **Rachel E. Lagenbacher**[1,2], **Dana Goerzen**[1,2], **Yue-Ming Li**[1,2], **Heeseon An**[1,2], **YuHuang Wang**[4,5] & **Daniel A. Heller**[1,2] ✉

Autophagy is a cellular process with important functions that drive neurodegenerative diseases and cancers. Lysosomal hyperacidification is a hallmark of autophagy. Lysosomal pH is currently measured by fluorescent probes in cell culture, but existing methods do not allow for quantitative, transient or in vivo measurements. In the present study, we developed near-infrared optical nanosensors using organic color centers (covalent sp^3 defects on carbon nanotubes) to measure autophagy-mediated endolysosomal hyperacidification in live cells and in vivo. The nanosensors localize to the lysosomes, where the emission band shifts in response to local pH, enabling spatial, dynamic and quantitative mapping of subtle changes in lysosomal pH. Using the sensor, we observed cellular and intratumoral hyperacidification on administration of mTORC1 and V-ATPase modulators, revealing that lysosomal acidification mirrors the dynamics of S6K dephosphorylation and LC3B lipidation while diverging from p62 degradation. This sensor enables the transient and in vivo monitoring of the autophagy–lysosomal pathway.

Lysosomes have emerged as essential signaling centers that govern cell growth, division and differentiation, as well as catabolic activity[1]. Dysregulated lysosomal function affects cell survival, invasion, immune evasion and drug resistance. Lysosomes play a large role in autophagy, a process that controls cellular homeostasis and the progression of many diseases. The impact of autophagy on cancers is heterogeneous[2,3]. Although autophagy increases immunosurveillance that suppresses tumor initiation, it also sustains cellular homeostasis and prevents chronic cellular damage in tumors. In ovarian carcinoma, for example, autophagy-related proteins are downregulated and autophagy activation can result in the death of these cancer cells[4,5].

Autophagic processes within tissues and whole organisms exhibit substantial complexities beyond those found in cell culture studies[3,6,7]. For instance, autophagy can be activated by hypoxic stress in the tumor microenvironment[8]. The role of autophagy differs throughout tumor development in response to dynamic changes in stresses such as nutrient deprivation, hypoxia and growth factor depletion in the microenvironment at different stages of progression[9,10]. Autophagy-mediated degradation of immune signaling proteins

---

[1]Memorial Sloan Kettering Cancer Center, New York, NY, USA. [2]Weill Cornell Medicine, Cornell University, New York, NY, USA. [3]Tri-Institutional PhD Program in Chemical Biology, Memorial Sloan Kettering Cancer Center, New York, NY, USA. [4]Department of Chemistry and Biochemistry, University of Maryland, College Park, MD, USA. [5]Maryland NanoCenter, University of Maryland, College Park, MD, USA. [6]Present address: School of Pharmacy, Faculty of Medicine, The Hebrew University of Jerusalem, Jerusalem, Israel. [7]These authors contributed equally: Mijin Kim, Chen Chen.
✉e-mail: hellerd@mskcc.org

helps tumors escape from both adaptive and innate immune system surveillance[11]. Thus, elucidation of the role of autophagy on cell signaling, dynamically and in vivo, would facilitate greater understanding of cancer progression and other disease processes. Autophagic flux is typically assessed by biochemical assays or fluorescent protein tagging of autophagy-related, ubiquitin-like protein ATG8 family members such as LC3B, autophagy substrates such as p62/SQSTM1 or other organellar markers in cells[12]. Assessments of autophagy and related processes in organisms generally require tissue acquisition at selected endpoints[7] or deletion of genes essential for the ATG8 conjugation pathway, such as ATG7 or ATG5 (refs. 13,14). The knockout of ATG7 or ATG5 in mice causes a defect in autophagosome formation, so it has been used to understand the physiological roles of autophagy. However, a permanent depletion of the autophagic pathway leads to neonatal lethality, organ failure and neurological dysfunction[15,16]. Alternatively, transgenic mice with systemic expression of green fluorescent protein-tagged LC3B were used to monitor autophagy in vivo[14]. Therefore, methods enabling dynamic and in vivo measurements of autophagy that do not require alterations in host tissues would provide important complementarity to facilitate mechanistic investigations and experimental therapeutics studies.

During the course of (macro)autophagy, a fusion event between lysosomes and autophagosomes exposes acid hydrolases to the autophagic cargoes for degradation. Acidic pH, generated by vacuolar H^+ ATPase (V-ATPase), is essential to facilitate lysosomal proteolysis and recycle damaged lysosomes, enhancing autophagic efficiency and lysosomal biogenesis. Lysosomal hyperacidification, subtle reductions in pH below the normal acidic levels of late endosomes/lysosomes, is regarded as a hallmark of autophagy. The mechanism of lysosomal hyperacidification is not fully understood[17]. There is a dearth of robust tools to quantify lysosomal pH in live cells and in vivo, however[18]. Existing lysosomal pH reporters include pH-sensitive microelectrodes[19], organic dyes[20,21], synthetic nanoparticles[22] and pH-sensitive fluorescent proteins[23]. Intracellular pH recordings using microelectrode tips are considered label free and enable high temporal resolution. However, the spatial resolution is limited by the size of the microelectrode tip and the measurement may disrupt cellular processes due to membrane puncturing. On the other hand, the most common method, fluorescent dyes, exhibits a time-dependent alkalizing effect on lysosomes[20,24], making temporal tracking of lysosomal pH, and in vivo use, challenging. Also, most optical probes are excited and emit at visible (380–700 nm) and first near-infrared (NIR-I, 700–900 nm) wavelengths where they exhibit phototoxicity[25,26] and shallow tissue penetration due to substantial tissue absorption and light scattering, and overlap with autofluorescence, limiting their use for in vivo imaging.

Semiconducting, single-walled carbon nanotubes (SWCNTs) exhibit electronic and optical properties that enable intracellular and in vivo imaging and sensing. SWCNT fluorescence exhibits narrow bandwidths (35–80 meV), allowing sensitive and precise quantification of local environments via quenching and solvatochromic responses and modulation of emission from quantum defect sites[27,28]. SWCNTs fluoresce in the second near-infrared window (NIR-II, 900–1700 nm)[29], where emission can penetrate living tissues to distances in the centimeter range with minimal light scattering and tissue absorbance[30]. Tissue autofluorescence drastically decreases at NIR-II wavelengths, improving contrast for in vivo imaging. SWCNT fluorescence (E_{11}) is highly photostable[31] and can be imaged in live cells, tissues and animals over long periods[31–33]. Noncovalent encapsulation with polymers, including short oligonucleotides, facilitates aqueous suspension and confers colloidal stability and biocompatibility in biological systems[34]. Organic color centers (OCCs) are molecularly tunable quantum defects on SWCNTs[35] that harvest mobile excitons to produce distinct, bright fluorescence bands (E_{11}^-) at longer wavelengths than the E_{11} peak. The E_{11}^- fluorescence of the OCC-functionalized SWCNTs (OCC–SWCNTs) introduces new biochemical sensitivities to SWCNTs determined by the chemical nature of the defect, making OCCs the molecular focal points for local environmental responses[36].

In the present study, we developed an optical nanosensor to measure autophagy-mediated, lysosomal hyperacidification events, quantitatively and temporally in live cells and in vivo. The sensors are composed of the *N,N*-diethyl-4-aminoaryl OCC modification of a SWCNT, encapsulated with an oligonucleotide. The nanosensor localized to the endolysosomal lumen where the emission of the OCCs responded via quantifiable wavelength shifts of the E_{11}^- band in response to local pH, whereas the E_{11} band remained largely stable, functioning as a reference. The nanosensor measured lysosomal pH changes on treatment with V-ATPase-targeting drugs and autophagy modulators in real time. Using NIR hyperspectral imaging, the nanosensor enabled the acquisition of quantitative maps of endolysosomal pH spatially, allowing direct comparisons between different cell types and experiments. We found that the nanosensor enables transient, spatial and noninvasive monitoring of pH, including subtle, autophagy-mediated hyperacidification, within tumors in live mice. Monitoring the intratumorally injected nanosensors enabled dynamic tracking of lysosomal pH on pharmacological modulation. The sensor revealed that lysosomal acidification mirrors dephosphorylation of S6 and lipidation of LC3B, exhibiting a sharp recovery after perturbation, whereas acidification diverged substantially from p62 degradation. These results suggest that pH temporally tracks mammalian target of rapamycin complex 1 (mTORC1) inhibition in the tumor microenvironment. This sensor technology constitutes a quantitative tool for discovery and preclinical investigations of lysosomal biology, autophagy and experimental therapeutics.

Results

OCC–DNA optical response to lysosomal pH

We developed pH-sensitive OCC–DNA complexes (Fig. 1a) and assessed their optical response. We covalently functionalized (6,5)-SWCNTs with an *N,N*-diethyl-4-aminobenzene diazonium salt in aqueous solution[36]. On successful functionalization, the fluorescence spectrum of OCC–SWCNTs exhibited a pair of emission peaks: the nanotube host emission (E_{11}) centered at 993 nm and the 'OCC peak' E_{11}^- at 1,149 nm (Supplementary Fig. 1). The E_{11}^- peak traced the titration curve of the aminobenzene group, shifting by 12 nm, whereas the E_{11} wavelength was nearly unchanged (<3 nm) in the pH range 3–8 (Fig. 1b). The E_{11}^- emission response is attributed to modulation of electronic resonance and inductive effects resulting from protonation of the amine group of the OCC[37].

We wrapped the OCC–SWCNTs with a single-stranded oligonucleotide that has the sequence $(GT)_{15}$, known to confer colloidal stability and biocompatibility even in the lysosome[38] (Methods and Supplementary Fig. 2). Successful DNA wrapping was confirmed by the periodic DNA pattern along the SWCNT axis, observed via atomic force microscopy (AFM; Fig. 1c). Both the optical and the chemical properties (quantum yield and pH responsivity) of OCC–SWCNTs were preserved after the DNA-wrapping process (Supplementary Fig. 3).

The optical properties of the resulting OCC–DNA complexes were characterized by fluorescence spectroscopy. On wrapping the OCC–SWCNTs with single-stranded (ss)$(GT)_{15}$, the E_{11} and E_{11}^- emission peaks redshifted by 6 nm, consistent with a shift in the absorbance band (Supplementary Fig. 4). We assessed the response of the OCC–DNA complexes to pH by observing the emission peak wavelength shift in various buffer/medium conditions with different pH values (Fig. 1d and Extended Data Fig. 1) . The variation of ΔE shifts in triplicate measurements was small. The maximum variation between repeat measurements of the same sample was <0.1 nm and small spectral shifts of <0.5 nm were easily identifiable. Multivalent metal ions, lipoproteins and small metabolites slightly shifted the OCC–DNA fluorescence wavelengths, but the pH sensitivity in the presence of these interferents remained consistent. Exposure to high concentrations of reactive

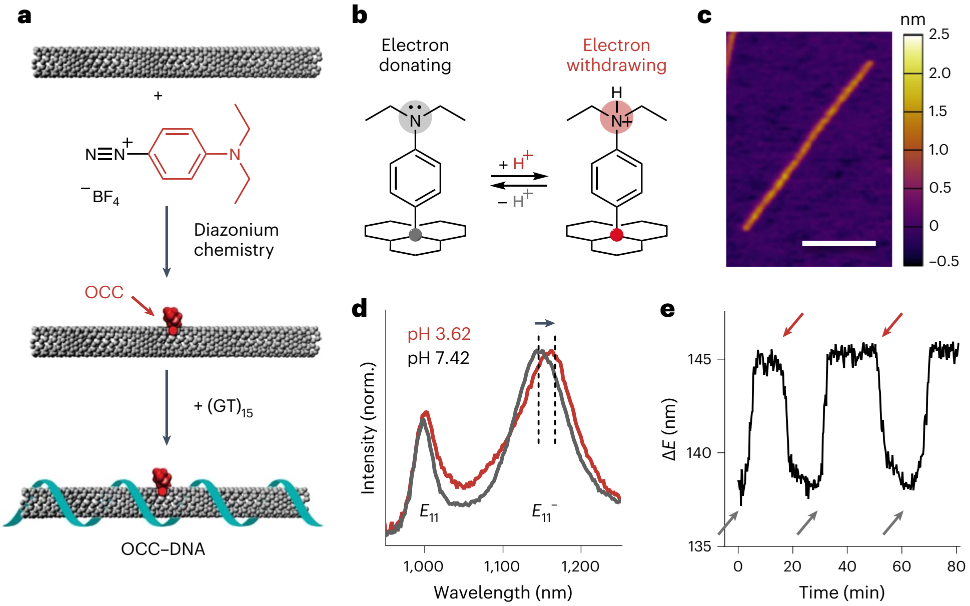

Fig. 1 | Synthesis of pH-responsive OCC–DNA complexes. a, Schematic of the synthesis of OCC–DNA complexes. **b**, Schematic of the molecular mechanism of response that involves mechanisms (protonation and deprotonation) of the *N*,*N*-diethylamino moieties group on the aryl OCC. **c**, AFM image of OCC–DNA complex. Scale bar, 100 nm. The color map denotes height. **d**, Representative NIR fluorescence spectra of OCC–DNA complexes in PBS at pH 3.14 (red) and pH 7.02 (gray) at 575-nm excitation. The arrow indicates the redshift of the E_{11}^- center wavelength in acidic buffer solution. **e**, Dynamics of the OCC–DNA response and reversal in buffer at pH 7.09 (gray arrows) and 3.32 (red arrows) at 575-nm excitation. The spectral shift $\Delta E = E_{11}^- - E_{11}$ is as measured from the emission peak center wavelengths. norm., normalized.

oxygen species (ROS), including hydrogen peroxide, superoxide radical anion or hydroxy radical, irreversibly inactivated the OCC–DNA complexes. This is attributed to the fact that 4-*N,N*-diethylaminoaryl OCC reacts with ROS to form a tertiary amine oxide that does not substantially modulate the electronic energy level of the defect state on protonation. In 20% fetal bovine serum (FBS), both E_{11} and E_{11}^- emission peaks redshifted approximately 1–2 nm, comprising a change in the baseline of the sensor but without changing the dynamic range of the pH response. This phenomenon is attributed to the exposure of the SWCNT to the electrostatic charges of proteins on their adsorption to the SWCNT sidewall[39].

The pH-responsive dynamic range of the OCC–DNA fluorescence depended on the protein composition and density (Extended Data Fig. 2), but the emission wavelength still responded quantitatively to solution pH within the physiological pH range (pH 3–7.4). Although the E_{11} peak wavelength exhibited <3-nm shifts on varying the pH from 7.4 to 3.5, the E_{11}^- wavelengths redshifted as high as 12 nm in protein-free buffer solutions. The dynamic range and wavelength shifts were independent of solution viscosity (Extended Data Fig. 3). To account for these protein-related effects, we used the E_{11} emission peak wavelength as an internal reference of the response. We thus reported the relative spectral shift of the OCC band, $\Delta E = E_{11}^- - E_{11}$ as the ultimate readout of pH response.

We then assessed the kinetics and reversibility of the OCC–DNA responses in phosphate-buffered saline (PBS) at pH values of 3.32 and 7.09 (Fig. 1e). The OCC–DNA complexes were loaded into a semipermeable poly(vinylidene fluoride) membrane capillary with a 500-kDa cut-off. The membrane was immersed in the buffer solution and the solution pH was modulated by alternatively exchanging acidic and basic buffer solutions every 20 min. The OCC–DNA emission through the membrane was continuously monitored. The Δ*E* exhibited immediate and reversible changes on pH modulation.

To assess long-term functionality in biological conditions, we incubated OCC–DNA complexes in 20% FBS at 37 °C for a week and compared the responsivity with fresh complexes (Supplementary Fig. 5). Although the intensity reduced by >80%, the pH sensitivity and peak wavelengths remained the same. The results suggest that the pH-responsive amine group of the OCCs does not easily degrade in biological environments.

To investigate the biocompatibility of the OCC–DNA complexes, we assessed dose-dependent cell viability. We used a human ovarian cancer cell line, SKOV3, to test the cell viability at a range of OCC–DNA concentrations (0–0.08 mg l^{-1}; Fig. 2a). The OCC–DNA complexes, incubated at up to 0.05 mg l^{-1} for 3 d, did not affect cell viability. We used 0.0015–0.01 mg l^{-1} as the working concentrations based on signal intensity in cells (Fig. 2b). At this concentration range, we observed OCC–DNA emission from individual puncta of the live cells in the hyperspectral imaging cube, suggesting that it is possible to obtain spatially resolved pH information. We did not observe rotational or tumbling motions of individual OCC–DNA complexes in the NIR videos of OCC–DNA complexes in live cells, suggesting that each punctum probably contained more than one OCC–DNA (Supplementary Video 1). We tested cell viability at the highest working concentration (0.01 mg l^{-1}) in several more cell lines, including human epithelial ovarian carcinoma (OVCAR3 and OVCAR8), human epithelial adenocarcinoma (HeLa), human epithelial kidney (HEK293T), mouse embryonic fibroblast (MEF) and mouse prostate cancer (RM1 and Myc-CaP) cells, and no cytotoxicity was observed (Extended Data Fig. 4). We also confirmed that 0.01 mg l^{-1} of OCC–DNA treatment did not induce NLRP3 inflammasome signaling (Supplementary Fig. 6).

We then investigated where the OCC–DNA complexes localized within live cells. We encapsulated OCC–SWCNTs with Cyanine5 (Cy5)-labeled ss$(GT)_{15}$ and treated the cells with 0.01 mg l^{-1} of the OCC–DNAs for 16 h. In confocal microscopy imaging, we observed that the Cy5 emission colocalized with the fluorescence of LysoTracker Green, which stains acidic compartments in cells (Fig. 2c). Quantitative colocalization analysis found a Manders' overlap coefficient between Cy5 and LysoTracker Green of 0.893 (±0.036) and the fraction of Cy5 emission overlapping LysoTracker emission was 0.988. These data suggest that the overwhelming majority of

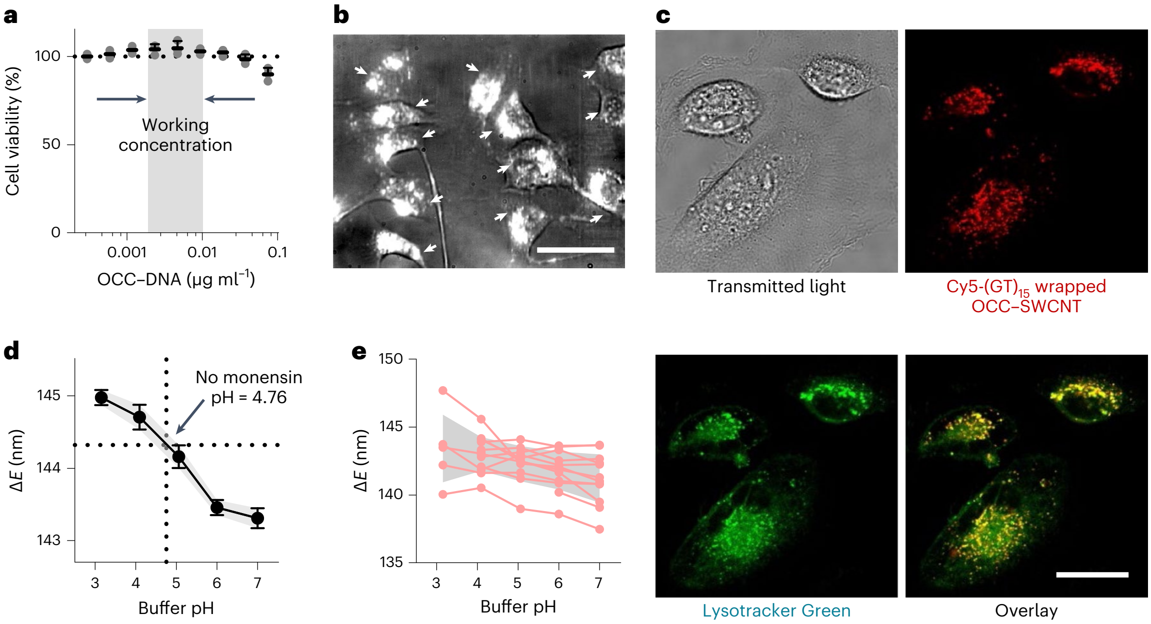

Fig. 2 | OCC–DNA complexes respond to endolysosomal pH. a, Viability of SKOV3 cells at increasing concentrations of OCC–DNAs, measured via CellTiter-Glo 2.0, after 72 h of incubation ($n = 3$). The data are presented as mean values with error bars as the s.d. The experiment was performed at least 3× with comparable results. **b**, Overlay of NIR emission of the OCC–DNA complexes from individual puncta of the live cells at 730-nm excitation and the transmitted light image. Arrows mark the 12 cells used for the OCC–DNA response analysis in **e**. Scale bar, 50 µm. **c**, Representative confocal microscopy images of Cy5-labeled OCC–SWCNT complexes (red) and LysoTracker Green (green) lysosomal imaging dye in live SKOV3 cells. Scale bar, 50 µm. **d**, OCC–DNA response in SKOV3 cells modulated by Hepes or MES buffer with monensin, measured under 730-nm excitation. Data are presented as mean values with error bars and error bands as the s.d. ($n = 25$). **e**, OCC–DNA response in each cell on exposure to buffer solutions of varying pH values with monensin. Each line denotes emission response obtained from 12 individual cells. The gray error band indicates the s.d. of the sensor responses.

OCC–DNA complexes were localized to the lysosomes. Based on the similar colocalization behavior of OCC–DNAs to underivatized DNA–SWCNTs (described extensively in Jena et al.[32]), we concluded that the OCC–DNA complexes behaved similarly to DNA–SWCNTs with respect to localization to the endolysosomal lumen. A significant reduction in cellular uptake of OCC–DNAs incubated at 4 °C, compared with 37 °C, suggests an energy-dependent, endocytic internalization mechanism (Supplementary Fig. 7). These similarities are anticipated based on the minor changes in the overall nanotube surface chemistry by the minimal functionalization with OCCs (one defect per 20 nm of SWCNT length).

To investigate lysosomal integrity in the presence of OCC–DNA complexes, we assessed cell viability with a lysosomotropic agent, L-leucyl-L-leucine methyl ester (LLOMe). No significant changes in LLOMe dose-dependent viability were observed between control and OCC–DNA-treated cells (Supplementary Fig. 8). In addition, the treatment of OCC–DNA complexes did not induce NLRP3 inflammation–downstream signaling of cathepsin release to cytosol by rupture and permeabilization of lysosomal membranes[40] (Supplementary Fig. 6). The median length of the OCC–DNA complexes was 252 nm (Supplementary Fig. 9) and lysosomes measured 0.1–1.2 µm in diameter[41,42]. However, endocytosis pathways can preferentially take up SWCNTs of certain sizes and largely reject particles that are too large for endosomes[43]. The results also agree with previous studies with DNA–SWCNTs[32], showing that they do not perturb the endolysosomal limiting membrane.

We then studied the effects of the OCC–DNAs on lysosomal function. We used the dye-quenched bovine serum albumin (DQ-BSA) assay, which measures lysosomal protein degradation activity. The assay confirmed that the OCC–DNA treatment did not alter lysosomal enzymatic function (Supplementary Fig. 10).

We measured the pH-induced peak shifts of the OCC–DNAs in live cells using NIR fluorescence spectroscopy (Supplementary Fig. 11). We treated SKOV3 cells with OCC–DNAs overnight and replaced with fresh medium 4 h before the spectroscopy measurement. The cells were then incubated in Hepes or MES (2-(*N*-morpholino)-ethanesulfonic acid) buffer with 10 µM of monensin (an ionophore that permeabilizes the lysosomal membrane and equilibrates the pH throughout the cell) in the pH range 3–7.4 for 10 min before acquiring fluorescence spectra of ensemble emission of the OCC–DNA complexes within the live cells at 575-nm excitation (Fig. 2d). A gradual increase in Δ*E* was observed as the cells were exposed to acidic buffer solutions. We also tracked the sensor response at the individual cell level at varying buffer pH conditions using hyperspectral NIR fluorescence microscopy[44]. The emission analysis showed that the Δ*E* shift and the dynamic range of pH responsivity were consistent with the spectral measurements of Fig. 2d (Fig. 2e).

To evaluate the pH response of OCC–DNAs on permeabilized lysosomes, we obtained OCC–DNA responses on 2-h treatment of 10 mM LLOMe in SKOV3 cells (Supplementary Fig. 12). The pH responsivity in the presence/absence of LLOMe remained the same. The lysosomal pH basified by 1.30 pH units in OCC–DNA/LLOMe cotreated cells, suggesting that permeabilization by LLOMe basified lysosomes close to cytosolic pH and treatment with OCC–DNA complexes alone maintained the lysosomal pH in the expected range[45].

We examined the OCC–DNA response to pH across different cell lines. We found that, although the wavelength shifts were qualitatively consistent, the dynamic range differed to some extent by cell type (Extended Data Fig. 5). Therefore, a specific titration curve for each cell line was used to interpolate the estimated lysosomal pH in all live-cell imaging and screening experiments. Based on the above experiments, we concluded that the OCC–DNA complexes constituted a sensor with

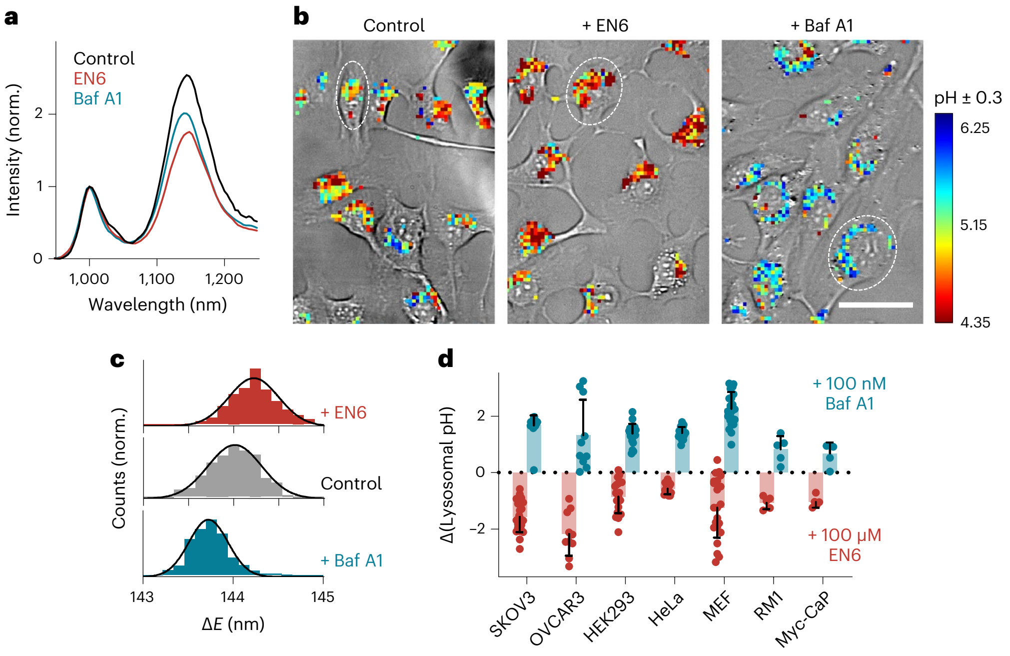

Fig. 3 | Nanosensor response under modulation of V-ATPase in live cells. **a**, NIR fluorescence emission spectra of regions of interest (ROIs) in the images in **b**. Each ROI is marked with a dashed circle. **b**, Maps of the nanosensor pH response in SKOV3 cells, as measured by NIR hyperspectral microscopy at 730-nm excitation, overlaid on to brightfield images 4 h after the introduction of DMSO (control), EN6 (100 µM) or Baf A1 (100 nM). Scale bar, 50 µm. **c**, Histogram of Δ*E* from all pixels with sensor emission from the hyperspectral images of cells in **b**. **d**, Lysosomal pH changes estimated from Δ*E* values from fluorescence spectroscopy measurements after 4-h drug treatment in seven different cell lines (*n* = 24, 10, 22, 19, 24, 5 and 5 spectra acquired for each condition, from the left to right cell lines, respectively). The bars are presented as mean values with error bars as the s.d.

the parameters defined by these experiments. We thus called the complexes a ‘sensor’ or ‘nanosensor(s)’ in the following studies.

The pH response to modulation of V-ATPase and mTORC1 activity

To measure lysosomal pH under pharmacological perturbations, we assessed the nanosensor response in cells treated with V-ATPase modulators bafilomycin A1 (Baf A1) and EN6. V-ATPase is a proton pump directly responsible for maintaining acidic pH in lysosomes. Baf A1 is a V-ATPase inhibitor that increases the lysosomal pH and is commonly used to block the fusion between autophagosomes and lysosomes[46,47]. EN6 covalently binds the ATPV1A subunit, which decouples the V-ATPase from the Ragulator complex, a pentameric protein complex that recruits mTORC1 to the lysosomal surface for activation. This leads to the inhibition of mTORC1 signaling and additionally increases the catalytic activity of V-ATPase[48]. V-ATPase plays a vital role in Rag-mTORC1-related autophagy activation[17]. Rag family proteins are direct recruiters for mTORC1 on the lysosome surface and control the activation state of mTORC1 (ref. 17). We first confirmed that the nanosensors remained inside the lysosomes regardless of the drug treatment and can report drug-induced endolysosomal pH changes (Supplementary Fig. 13). Colocalization analysis indicates that the average fraction of nanosensor emission overlapping emission from the lysosomal dye, LysoTracker Green, does not significantly vary between treatment conditions.

We acquired the sensor responses within SKOV3 cells under 100 nM Baf A1 and 100 µM EN6 treatments using NIR hyperspectral microscopy. The sensor emission spectra from individual cells showed blueshifted peak wavelengths for Baf A1 and redshifted peak wavelengths for EN6, compared with the control (Fig. 3a). The spatially resolved emission from the nanosensors facilitated the production of quantitative, live-cell maps of lysosomal pH (Fig. 3b). In SKOV3 cells, the mean of the Δ*E* distribution decreased by 0.6 nm under Baf A1 treatment and increased 0.5 nm on EN6 treatment, indicating lysosomal basification from pH 5.15 to pH 6.15 and acidification to pH 4.35 in each treatment condition, respectively (Fig. 3c).

Via NIR fluorescence spectroscopy of wells in a 96-well plate, we measured the ensemble fluorescence emission of the sensors from within adhered cells. After a 4-h treatment with 100 µM EN6, we observed a 0.8-nm increase in Δ*E*, corresponding to lysosomal acidification from pH 4.93 to pH 3.38 (Fig. 3d). Conversely, 100 nM Baf A1 resulted in a 1.22-nm attenuation of Δ*E*, corresponding to the lysosomal basification to pH 6.51. Using the DQ-BSA assay, we found elevated and reduced enzymatic activities of lysosomes on EN6 and Baf A1 treatments, respectively (Supplementary Fig. 14), as expected[49,50]. We also measured the sensor emission in six additional cell lines under 4-h treatments of EN6 and Baf A1. The Δ*E* and lysosomal pH responses were qualitatively consistent, further validating the sensor functionality in live cells.

We used the nanosensor to dynamically measure pH changes on pharmacological perturbation. Continuous monitoring of the sensor emission resulted in transient quantification of lysosomal pH in SKOV3 cells (Fig. 4a). Baf A1 caused immediate lysosomal basification, which equilibrated before the first data point at 15 min, consistent with the known mechanism of action[46,47]. The introduction of EN6 to the medium resulted in acidification of the lysosomes, which began within minutes. This rapid response suggests that EN6 induces lysosomal pH changes in these cells due to the direct modulation of catalytic efficiency of V-ATPase rather than the modulation of V-ATPase expression levels by the mTORC1 inhibition and transcription factor EB (TFEB) translocation, which becomes evident only after several hours[51].

We studied the relationship between EN6-induced lysosomal acidification and autophagy flux in SKOV3 cells. A dose-dependent increase in autophagy activation was observed on 4-h treatment with

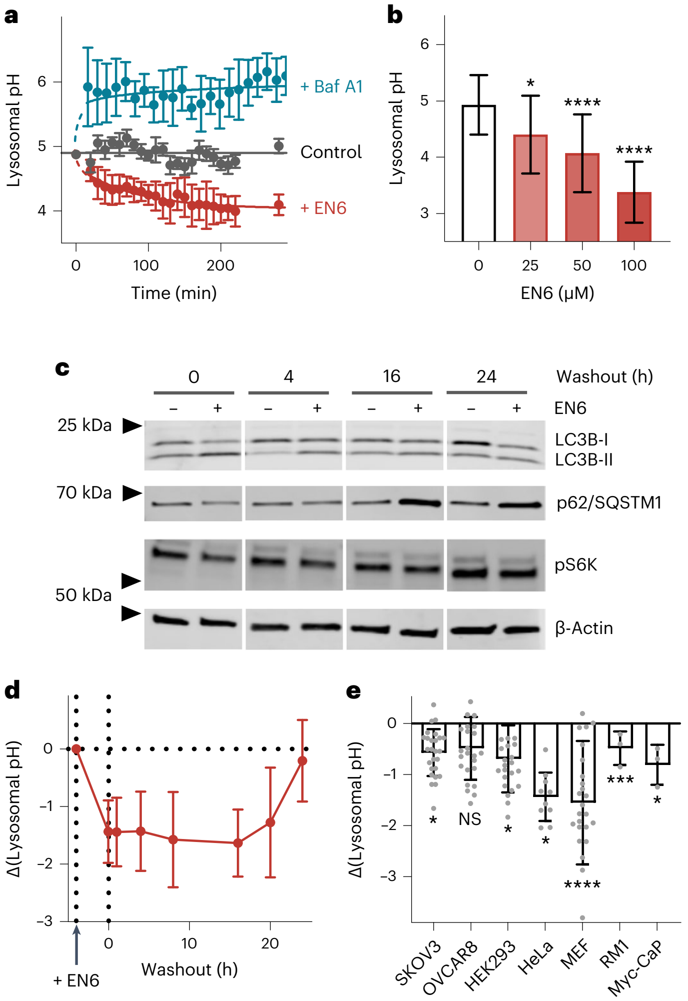

Fig. 4 | Dynamic response to V-ATPase and mTORC modulation in live cells. **a**, Time-dependent lysosomal pH in response to EN6 (red), Baf A1 (blue) or control (black) treatment conditions in SKOV3 cells ($n = 3$ spectra). **b**, Dose-dependent lysosomal pH response in SKOV3 cells on 4 h of treatment with EN6. $^{*}P = 0.0147$, $^{****}P < 0.0001$ ($n = 20$ for DMSO and 25 for EN6 treatments). **c**, Time-dependent expression of autophagy and mTORC signaling effectors in SKOV3 cells on introduction and washout of EN6. Western blotting was performed at least 3× with comparable results. **d**, Time-dependent pH response of nanosensors in SKOV3 cells to 100 μM EN6 treatment for 4 h and washout ($n = 25$). **e**, Change in lysosomal pH on 4-h treatment of 250 nM torin 1, with respect to DMSO control ($n = 26, 25, 24, 10, 26, 3$ and 3, from left to right cell lines, respectively). $^{*}0.005 < P < 0.05$, $^{***}P = 0.0005$, $^{****}P < 0.0001$; NS, not significant. All data are presented as mean values with error bars as the s.d. (**a**,**b**,**d**,**e**), and statistical significance was analyzed using a one-way analysis of variance (ANOVA) followed by Dunnett's multiple-comparison test (**b**,**e**). All experiments were performed at least 3× with comparable results.

EN6 via western blotting (Supplementary Fig. 15). On increasing concentrations of EN6, the level of phosphorylated canonical substrate S6 kinase 1 (pS6K) gradually decreased, indicating the inactivation of mTORC1 signaling. The number of autophagosomes and autophagic flux increased, evidenced by the increased levels of conjugated LC3B-II and degradation of p62/SQSTM1 (sequestosome 1). We observed dose-dependent lysosomal acidification as measured by the nanosensor (Fig. 4b). The pH response was consistent with reports of lysosomal acidification concomitant with autophagy activation[48].

We further interrogated the dynamics of the V-ATPase-specific autophagy activator, EN6, in SKOV3 cells. We conducted a washout experiment to assess both EN6-induced autophagy activation and lysosomal pH modulation and reversal. The cells were exposed to 100 μM EN6 for 4 h, then washed out and grown in fresh medium free of EN6. Autophagy markers were measured after washout. We observed that LC3B-II and pS6K returned to the untreated levels after 16 h, whereas V-ATPase expression did not change in response to the drug (Fig. 4c and Supplementary Fig. 16). In parallel, we measured the nanosensor emission to estimate the lysosomal pH at each time point (Fig. 4d). The lysosomes maintained a pH of approximately 3.75 up to 16 h, before starting to recover the basal lysosomal pH of 4.93, which fully returned to baseline levels 24 h post-washout. The prolonged effects of lysosomal acidification and autophagy activation were attributed to the irreversible nature of the covalent modulator on the target. In addition, even 16 h after washout, we observed persistent effects of EN6. We surmise that EN6-bound V-ATPase gradually turned over in 16 h; newly synthesized V-ATPases started to restore the lysosomal pH and mTORC1 was recruited back to the lysosomes. We also observed that the levels of p62/SQSTM1 decreased after EN6 washout and were restored after 4 h but then increased after 16 h, probably due to the feedback effects on TFEB[52]. TFEB directly regulates p62/SQSTM1, the expression level of which increases similar to cells under prolonged starvation because covalently bound EN6 continued to inhibit mTORC1 even after washout.

We investigated lysosomal pH modulation due to mTORC1/2 inhibition by torin 1. Torin 1 is a potent autophagy activator that directly competes with the ATP-binding pocket in mTORC1/2 (ref. 53) We observed lysosomal acidification within 4 h of torin 1 treatment at a concentration of 250 nM, where the degree of acidification was cell-type dependent (Fig. 4e). Consistent with the previous reports, torin 1 acidified the lysosomal pH in HeLa and MEF cells. The prostate cancer cell lines, Myc-CaP and RM1, human ovarian cancer cells, SKOV3 and OVCAR8, and HEK293T cells exhibited relatively small decreases in lysosomal pH. Concomitantly, autophagy markers confirmed autophagy activation on torin 1 treatment (Supplementary Fig. 17). The results suggest that divergent responses of lysosomal activity on autophagy activation may explain the heterogeneous sensitivities of autophagic processes in different cell types and the time course of autophagy can be monitored by the nanosensors.

We assessed inhibitor-mediated modulation of the nanosensor response. The emission wavelength shifted, but the dynamic range remained the same, when cells were treated with torin 1 but not with the other inhibitors (Extended Data Fig. 6). We thus applied a new calibration curve to correct the lysosomal pH change on torin 1 treatment. We hypothesized that the torin 1-mediated OCC–DNA response derived from autophagy activation-induced accumulation of proteins in the lysosome, which influenced the local electrostatic environment in the lysosomes, and thus the optical bandgap of SWCNTs[39], as described heretofore (Extended Data Fig. 2). We thus assessed torin 1-induced shifting of the nanosensor response in autophagy-defective, ATG7$^{-/-}$ HEK293T cells (Extended Data Fig. 7). We found that knocking out ATG7 abrogated the differences in OCC–DNA response. As ATG7 knockout prevents mTORC1/2 inhibition-mediated autophagy activation and concomitant changes in lysosomal composition[1,17], the results suggest that a large influx of cargo proteins can cause modulation of the OCC–DNA wavelength.

In vivo, quantitative, dynamic imaging of the pH response

We investigated the nanosensor in vivo using a xenograft model of ovarian cancer. Nanosensors were injected intratumorally into SKOV3 tumors when they reached 120 mm^3 (Fig. 5a). Emission spectra of the sensors were obtained starting 24 h after injection using an NIR hyperspectral mouse imager (Supplementary Fig. 18). Strong nanosensor fluorescence was detected within tumors (Fig. 5b), which gradually decreased by 35% after 3 d (Extended Data Fig. 8). We note that the intensity attenuation was not statistically significant during the measurements. Immunofluorescence imaging of lysosome-associated

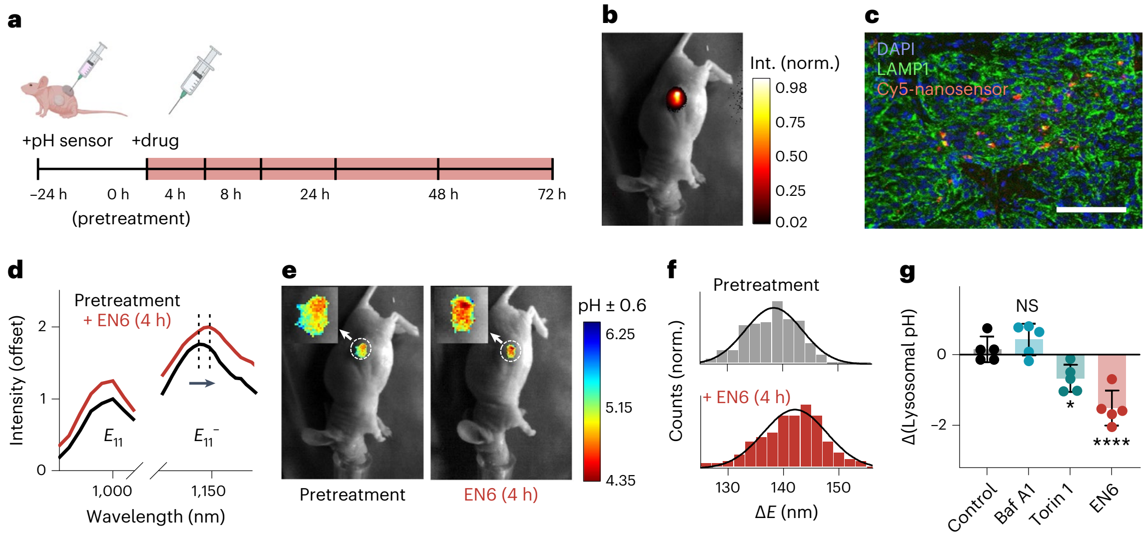

Fig. 5 | In vivo nanosensor response to V-ATPase and mTORC modulation. **a**, Experimental scheme used here and in Fig. 6. **b**, Overlay of transmitted light and NIR fluorescence emission of the nanosensors in vivo in a mouse with SKOV3 tumor 24 h after the sensor injection (30 µl of the nanosensors in PBS, 0.1 mg l^{-1}). Int., Intensity. **c**, Overlay of the Cy5-labeled nanosensors (red), LAMP1 (green) and DAPI (blue) from a tumor slice 24 h after the sensor injection. Scale bar, 100 µm. **d**, Averaged sensor emission from the mouse tumor before and after EN6 treatment at 808-nm excitation. The selected ROIs are marked with a dashed circle in **e**. **e**, Overlay of transmitted light and hyperspectral wavelength analysis images in vivo before (left) and after (right) EN6 treatment in the same mouse as in **b**. **f**, Histogram of ΔE from all pixels with sensor emission from the hyperspectral images of solid tumors in **d**. **g**, Lysosomal pH change 4 h after the drug treatment ($n = 5$ biological replicates per group). Statistical significance was analyzed using a one-way ANOVA followed by Dunnett's multiple-comparison test. $^{*}P = 0.0206$, $^{****}P < 0.001$. The data are presented as mean values with error bars as the s.d.

membrane glycoprotein 1 (LAMP1) was conducted in Cy5-labeled, nanosensor-injected tumor slices (Fig. 5c). Adjacent, 5-µm sections were required for tissue imaging, due to the need to protect the labeled nanosensor emission during the staining protocol. Quantitative analysis revealed that the fraction of Cy5 (nanosensor) emission colocalized with LAMP1 signal was 0.715. A small fraction of Cy5 signal (0.083) was adjacent to LAMP1 emission but not overlapping. Cy5 colocalized with DAPI to a small degree (0.210) and a minor fraction of LAMP1 emission overlapped with DAPI (0.202) as well. We believe that the 5-µm thickness of the slices led to unexpected colocalization between DAPI and LAMP1/Cy5 and the limited *z*-resolution, which were not of concern in the live-cell colocalization study (Fig. 2c). We did not find significant Cy5 emission in the extratumoral space. We, therefore, conclude that the nanosensors localized largely to late endosomes or lysosomes in the tumor cells in vivo. The hematoxylin and eosin-stained tissues were assessed by a trained pathologist; no signs of injury or other abnormalities were found in the tumor tissues on intratumoral injection of the sensor (Supplementary Fig. 19).

We measured the intratumoral pH response of the nanosensor to autophagy modulators in vivo. Mice were randomized into four treatment groups 24 h after nanosensor injection. Mice were administered EN6 (50 m kg^{-1}), Baf A1 (0.125 mg kg^{-1}), torin 1 (20 mg kg^{-1}) or vehicle (saline:dimethylsulfoxide (DMSO):Poly(ethylene glycol) 400 (PEG 400), v:v:v = 6:1:1) intraperitoneally. The sensor response from the solid tumors was monitored for 72 h. The emission wavelength remained stable over the experiments for the control group, denoting no significant pH changes. The in vivo spectra showed distinct red shifts in the EN6 treatment group (Fig. 5d). We employed the in vitro calibration curve to estimate the actual lysosomal pH from the ΔE values in vivo. Due to the low spectral resolution in the E_{11} peak (10 nm), the variation in estimated pH was larger than in the cell experiments (|max. error| < pH 0.6 unit), but the sensor response was qualitatively consistent with the results of the live-cell experiments (Fig. 5e). Within 4 h of the EN6 treatment, the nanosensors reported statistically significant redshifting in the E_{11}^{-} wavelength and increased ΔE (Fig. 5f), indicating lysosomal acidification in the tumor from pH 5.15 to pH 4.35 (Fig. 5g).

We measured the intratumoral dynamics of lysosomal pH modulation in vivo. Lysosomes of the SKOV3 xenograft tumor cells acidified within 4 h and returned to normal levels 24 h after EN6 treatment (Fig. 6a). Torin 1 treatment elicited a smaller but significant lysosomal acidification event (Fig. 6b). Lysosomal pH remained low for 24 h before starting to recover. Baf A1 treatment elicited the opposite change in E_{11}^{-} emission wavelength as expected, although the change was not statistically significant. We also assessed the effectors of the drugs in the tumors. EN6 and torin 1 treatments both inhibited mTORC1 signaling as demonstrated by reduced phosphorylation of S6 in the tumor tissues (Fig. 6c), whereas autophagy was activated, evinced by reduced p62/SQSTM1 levels (Fig. 6d) in immunohistochemical stains (Supplementary Figs. 20–22). The timeframe of pS6 reduction and reversal (and thus mTORC1 activity) closely followed that of lysosomal acidification. However, p62/SQSTM1 levels decreased within 4 h and remained low over 72 h. The dynamics of the lysosomal pH in vivo was consistent with the in vitro washout experiment of EN6 (Fig. 4c,d). The onset of lysosomal acidification mirrored the attenuation of pS6, an indication of reduced mTORC1 activity. Conversely, lysosomal pH dynamics diverged from downstream autophagy signaling (p62/SQSTM1).

Discussion

We developed an optical nanosensor that enabled quantitative and dynamic monitoring of endolysosomal pH in live cells and in vivo. The nanosensor reported lysosomal pH changes induced by modulation of the catalytic activity of V-ATPase and mTORC1 inhibition in various cell lines. Using the method, we found sustained pH dysregulation induced by covalent targeting of V-ATPase in live cells and provided dynamic measurements of intratumoral lysosomal pH in vivo. We also found that autophagy modulators induced pronounced differences in lysosomal acidification, depending on the cell type. The results suggest that pH dysregulation may correspond with heterogeneous responses

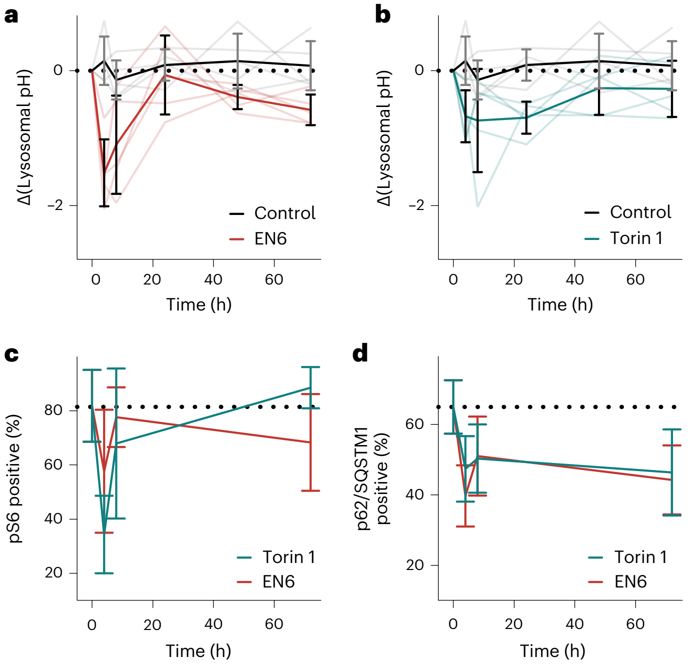

Fig. 6 | In vivo dynamic monitoring of autophagy induction. **a**,**b**, Time-dependent lysosomal pH in control versus EN6 (50 mg kg^{-1}) (**a**) and torin 1 (20 mg kg^{-1}) (**b**) treatment groups. Opaque lines denote mean values and transparent lines individual datasets ($n = 5$ biological replicates per group). **c**,**d**, Quantitative histology image analysis of phosphorylated S6 (**c**) and p62/SQSTM1-positive (**d**) cells with EN6 or torin 1 treatment groups. The DMSO control is considered as 0-h treatment ($n = 11$ immunohistochemistry images for five biological replicates per group). All data are presented as mean values with error bars as the s.d. (**a**–**d**).

of autophagy activation among cancers and certain autophagic vulnerabilities in cancer cells may result from lysosomal dysregulation. Further investigations, regarding the signaling pathways regulating autophagy-related lysosomal hyperacidification and the degree and causes of any divergence from the canonical acidification behavior among cancer cells, are warranted[17].

Experiments in live cells revealed that lysosomal pH dynamics mirrored dephosphorylation of S6K and lipidation of LC3B on autophagy activation, but that pH desynchronized with p62/SQSTM1 degradation. In vivo, lysosomal pH was concomitant with pS6 but again diverged from p62/SQSTM1. The results suggest that lysosomal hyperacidification, a hallmark of autophagy, is an indicator of mTORC1 inhibition.

We found that this method can dynamically assess autophagy-associated processes by monitoring lysosomal hyperacidification in vivo, addressing certain limitations of current autophagy assays[7,12]. Molecular markers such as p62/SQSTM1 and LC3B for autophagy monitoring, through either western blotting or fluorescent protein tags, currently provide the most direct measurements of autophagic flux. However, the dynamic process of autophagy may not be fully captured by static imaging[7]. For instance, enhanced autophagic flux facilitates the degradation of p62/SQSTM1 but also upregulates the expression through TFEB and autophagy-derived amino acids[54]. Hydrolase activity assays such as DQ-BSA provide a high-throughput readout for autophagic screenings. However, different hydrolases perform optimally under different pH values and whether more efficient cleavage of a universal fluorescent marker is directly related to autophagy flux is still in question. In vivo applications using these bioassays are even more challenging due to the limitations of using these probes in living tissues. We found that the nanosensor can monitor the fluctuation of the tumor autophagy (or lysosomal) activity to facilitate investigation without the need for permanent alteration of the autophagy signaling in host and/or tumor, complementing studies using transgenic mouse models.

We provide an assessment of the limitations of this technology. The nanosensors currently measure pH only within the endolysosomal pathway. To produce quantitative pH measurements/maps within cell lines, calibration curves must be obtained using each cell line. Cell-type-dependent variation in nanosensor responses may be attributed to changes in lysosomal protein content and/or ionic strength[39,55]. In addition, certain perturbations can result in modulation of the sensor response, such as drugs that cause large changes in the protein/nutrient content of the lysosome, as we found with strong mTORC1/2 inhibition. Similar challenges have been identified with pH-sensitive fluorescent dyes[56] and such modulations must similarly be accounted for by acquiring calibration curves in the presence of the perturbation, potentially as part of a validation study in the case of drug-screening investigations. With regard to the instrumentation required to use the nanosensor, conventional plate readers and microscopes that can measure fluorescence signals of conventional bioanalytical pH sensors cannot be used, although compatible instruments, incorporating an NIR detector, are now commercially available[33,44]. Such detectors have been incorporated into plate readers[39] and, in addition, hyperspectral imaging devices (for spatial pH mapping) have been integrated into fluorescence microscopes[44] and in vivo animal imaging systems[33]. For rapid measurements, a fiberoptic-based probe system can be used to measure the sensor fluorescence noninvasively in live mice in ≤5 s per mouse[55].

Our findings suggest that it can be used generally for quantitative imaging and high-throughput measurements. The sensitivity is sufficient for measuring the lysosomal acidification/basification activities of autophagy-mediated hyperacidification in multiple cell lines/in vivo. High-throughput measurements of sensor response in multiple experimental conditions were performed in a 96-well plate format. With regard to the dynamic measurements, we found that the response of the sensor itself is immediate. For long-term measurements, the technology captured the dynamic pH response across 24 h. In vivo studies demonstrated spatiotemporal imaging of drug action in live animals and longitudinal assessment of endolysosomal pH in the same mice for up to 72 h. We anticipate that this technology will facilitate the understanding of the regulatory mechanisms of dysregulated biological systems in disease and accelerate the discovery of new therapeutic targets and interventions.

Online content

Any methods, additional references, Nature Portfolio reporting summaries, source data, extended data, supplementary information, acknowledgements, peer review information; details of author contributions and competing interests; and statements of data and code availability are available at https://doi.org/10.1038/s41589-023-01364-9.

References

1. Lawrence, R. E. & Zoncu, R. The lysosome as a cellular centre for signalling, metabolism and quality control. *Nat. Cell Biol.* **21**, 133–142 (2019).
2. Mulcahy Levy, J. M. & Thorburn, A. Autophagy in cancer: moving from understanding mechanism to improving therapy responses in patients. *Cell Death Differ.* **27**, 843–857 (2020).
3. Galluzzi, L. et al. Autophagy in malignant transformation and cancer progression. *EMBO J.* **34**, 856–880 (2015).
4. Zhan, L. et al. Autophagy as an emerging therapy target for ovarian carcinoma. *OncoTarget* **7**, 83476–83487 (2016).
5. Jung, S., Jeong, H. & Yu, S.-W. Autophagy as a decisive process for cell death. *Exp. Mol. Med.* **52**, 921–930 (2020).
6. Lauzier, A. et al. Colorectal cancer cells respond differentially to autophagy inhibition in vivo. *Sci. Rep.* **9**, 11316 (2019).

7. Klionsky, D. J. et al. Guidelines for the use and interpretation of assays for monitoring autophagy (4th edition). *Autophagy* **17**, 1–382 (2021).
8. Bellot, G. et al. Hypoxia-induced autophagy is mediated through hypoxia-inducible factor induction of BNIP3 and BNIP3L via their BH3 domains. *Mol. Cell. Biol.* **29**, 2570–2581 (2009).
9. Chavez-Dominguez, R., Perez-Medina, M., Lopez-Gonzalez, J. S., Galicia-Velasco, M. & Aguilar-Cazares, D. The double-edge sword of autophagy in cancer: from tumor suppression to pro-tumor activity. *Front. Oncol.* **10**, 578418 (2020).
10. Kimmelman, A. C. & White, E. Autophagy and tumor metabolism. *Cell Metab.* **25**, 1037–1043 (2017).
11. Janji, B., Berchem, G. & Chouaib, S. Targeting autophagy in the tumor microenvironment: new challenges and opportunities for regulating tumor immunity. *Front. Immunol.* **9**, 887 (2018).
12. Mizushima, N. & Murphy, L. O. Autophagy assays for biological discovery and therapeutic development. *Trends Biochem. Sci.* **45**, 1080–1093 (2020).
13. Poillet-Perez, L. et al. Autophagy promotes growth of tumors with high mutational burden by inhibiting a T-cell immune response. *Nat. Cancer* **1**, 923–934 (2020).
14. Kuma, A., Komatsu, M. & Mizushima, N. Autophagy-monitoring and autophagy-deficient mice. *Autophagy* **13**, 1619–1628 (2017).
15. Yoshii, SaoriR. et al. Systemic analysis of Atg5-null mice rescued from neonatal lethality by transgenic ATG5 expression in neurons. *Dev. Cell* **39**, 116–130 (2016).
16. Karsli-Uzunbas, G. et al. Autophagy is required for glucose homeostasis and lung tumor maintenance. *Cancer Discov.* **4**, 914–927 (2014).
17. Yim, W. W.-Y. & Mizushima, N. Lysosome biology in autophagy. *Cell Discov.* **6**, 6 (2020).
18. Williams, R. M. et al. Harnessing nanotechnology to expand the toolbox of chemical biology. *Nat. Chem. Biol.* **17**, 129–137 (2021).
19. Aref, M. et al. Potentiometric pH nanosensor for intracellular measurements: real-time and continuous assessment of local gradients. *Anal. Chem.* **93**, 15744–15751 (2021).
20. Ma, L., Ouyang, Q., Werthmann, G. C., Thompson, H. M. & Morrow, E. M. Live-cell microscopy and fluorescence-based measurement of luminal pH in intracellular organelles. *Front. Cell Dev. Biol.* **5**, 71 (2017).
21. Myochin, T. et al. Rational design of ratiometric near-infrared fluorescent pH probes with various pK_a values, based on aminocyanine. *J. Am. Chem. Soc.* **133**, 3401–3409 (2011).
22. Robinson, K. J. et al. Modified organosilica core–shell nanoparticles for stable pH sensing in biological solutions. *ACS Sens.* **3**, 967–975 (2018).
23. Burgstaller, S. et al. pH-lemon, a fluorescent protein-based pH reporter for acidic compartments. *ACS Sens.* **4**, 883–891 (2019).
24. Guha, S. et al. Approaches for detecting lysosomal alkalinization and impaired degradation in fresh and cultured RPE cells: evidence for a role in retinal degenerations. *Exp. Eye Res.* **126**, 68–76 (2014).
25. Wäldchen, S., Lehmann, J., Klein, T., van de Linde, S. & Sauer, M. Light-induced cell damage in live-cell super-resolution microscopy. *Sci. Rep.* **5**, 15348 (2015).
26. Laissue, P. P., Alghamdi, R. A., Tomancak, P., Reynaud, E. G. & Shroff, H. Assessing phototoxicity in live fluorescence imaging. *Nat. Methods* **14**, 657–661 (2017).
27. Heller, D. A. et al. Peptide secondary structure modulates single-walled carbon nanotube fluorescence as a chaperone sensor for nitroaromatics. *Proc. Natl Acad. Sci. USA* **108**, 8544–8549 (2011).
28. Kim, M. et al. Detection of ovarian cancer via the spectral fingerprinting of quantum-defect-modified carbon nanotubes in serum by machine learning. *Nat. Biomed. Eng.* **6**, 267–275 (2022).
29. Bachilo, S. M. et al. Structure-assigned optical spectra of single-walled carbon nanotubes. *Science* **298**, 2361 (2002).
30. Welsher, K., Sherlock, S. P. & Dai, H. Deep-tissue anatomical imaging of mice using carbon nanotube fluorophores in the second near-infrared window. *Proc. Natl Acad. Sci. USA* **108**, 8943 (2011).
31. Mandal, A. K. et al. Fluorescent sp^3 defect-tailored carbon nanotubes enable NIR-II single particle imaging in live brain slices at ultra-low excitation doses. *Sci. Rep.* **10**, 5286 (2020).
32. Jena, P. V. et al. A carbon nanotube optical reporter maps endolysosomal lipid flux. *ACS Nano* **11**, 10689–10703 (2017).
33. Galassi, T. V. et al. An optical nanoreporter of endolysosomal lipid accumulation reveals enduring effects of diet on hepatic macrophages in vivo. *Sci. Transl. Med.* **10**, eaar2680 (2018).
34. Galassi, T. V. et al. Long-term in vivo biocompatibility of single-walled carbon nanotubes. *PLoS ONE* **15**, e0226791 (2020).
35. Brozena, A. H., Kim, M., Powell, L. R. & Wang, Y. Controlling the optical properties of carbon nanotubes with organic colour-centre quantum defects. *Nat. Rev. Chem.* **3**, 375–392 (2019).
36. Kwon, H. et al. Optical probing of local pH and temperature in complex fluids with covalently functionalized, semiconducting carbon nanotubes. *J. Phys. Chem. C* **119**, 3733–3739 (2015).
37. Piao, Y. et al. Brightening of carbon nanotube photoluminescence through the incorporation of sp^3 defects. *Nat. Chem.* **5**, 840–845 (2013).
38. Gravely, M., Safaee, M. M. & Roxbury, D. Biomolecular functionalization of a nanomaterial to control stability and retention within live cells. *Nano Lett.* **19**, 6203–6212 (2019).
39. Roxbury, D., Jena, P. V., Shamay, Y., Horoszko, C. P. & Heller, D. A. Cell membrane proteins modulate the carbon nanotube optical bandgap via surface charge accumulation. *ACS Nano* **10**, 499–506 (2016).
40. Hornung, V. et al. Silica crystals and aluminum salts activate the NALP3 inflammasome through phagosomal destabilization. *Nat. Immunol.* **9**, 847–856 (2008).
41. Holtzmann, E. *Lysosomes* (Plenum, 1989).
42. Alberts, B. et al. *Molecular Biology of the Cell*, 4th edn (Garland Science, 2002).
43. Jin, H., Heller, D. A., Sharma, R. & Strano, M. S. Size-dependent cellular uptake and expulsion of single-walled carbon nanotubes: single particle tracking and a generic uptake model for nanoparticles. *ACS Nano* **3**, 149–158 (2009).
44. Roxbury, D. et al. Hyperspectral microscopy of near-infrared fluorescence enables 17-chirality carbon nanotube imaging. *Sci. Rep.* **5**, 14167 (2015).
45. Han, J. & Burgess, K. Fluorescent indicators for intracellular pH. *Chem. Rev.* **110**, 2709–2728 (2010).
46. Yamamoto, A. et al. Bafilomycin A_1 prevents maturation of autophagic vacuoles by inhibiting fusion between autophagosomes and lysosomes in rat hepatoma cell line, H-4-II-E cells. *Cell Struct. Funct.* **23**, 33–42 (1998).
47. Mauvezin, C. & Neufeld, T. P. Bafilomycin A1 disrupts autophagic flux by inhibiting both V-ATPase-dependent acidification and Ca-P60A/SERCA-dependent autophagosome–lysosome fusion. *Autophagy* **11**, 1437–1438 (2015).
48. Chung, C. Y.-S. et al. Covalent targeting of the vacuolar H^+-ATPase activates autophagy via mTORC1 inhibition. *Nat. Chem. Biol.* **15**, 776–785 (2019).
49. Frost, L. S., Dhingra, A., Reyes-Reveles, J. & Boesze-Battaglia, K. The use of DQ-BSA to monitor the turnover of autophagy-associated cargo. *Methods Enzymol.* **587**, 43–54 (2017).
50. Corrotte, M., Fernandes, M. C., Tam, C. & Andrews, N. W. Toxin pores endocytosed during plasma membrane repair traffic into the lumen of MVBs for degradation. *Traffic* **13**, 483–494 (2012).

51. Peña-Llopis, S. et al. Regulation of TFEB and V-ATPases by mTORC1. *EMBO J.* **30**, 3242–3258 (2011).
52. Settembre, C. et al. TFEB links autophagy to lysosomal biogenesis. *Science* **332**, 1429 (2011).
53. Thoreen, C. C. et al. An ATP-competitive mammalian target of rapamycin inhibitor reveals rapamycin-resistant functions of mTORC1*. *J. Biol. Chem.* **284**, 8023–8032 (2009).
54. Sahani, M. H., Itakura, E. & Mizushima, N. Expression of the autophagy substrate SQSTM1/p62 is restored during prolonged starvation depending on transcriptional upregulation and autophagy-derived amino acids. *Autophagy* **10**, 431–441 (2014).
55. Harvey, J. D. et al. A carbon nanotube reporter of microRNA hybridization events in vivo. *Nat. Biomed. Eng.* **1**, 0041 (2017).
56. Zhang, X.-X. et al. pH-sensitive fluorescent dyes: are they really pH-sensitive in cells? *Mol. Pharm.* **10**, 1910–1917 (2013).

Methods

Purification of (6,5)-SWCNT

Raw SWCNT material, CoMoCAT SG65i (Sigma-Aldrich) was dispersed in 1 w:v% sodium deoxycholate (DOC; Sigma-Aldrich, 99.9%) aqueous solution at a nanotube concentration of 1 mg ml^{-1} using tip sonication at 6 W (Sonics & Materials, Inc.) and 4 °C for 1 h, followed by ultracentrifugation at 100,000g for 30 min. The 85% supernatant was used to enrich (6,5)-SWCNT solution based on the previously reported protocol[57]. The final purified (6,5)-SWCNTs were stabilized in 1.04% DOC solution to maintain long-term colloidal stability (>6 months).

Covalent functionalization of purified (6,5)-SWCNTs

N,*N*-Diethylaminoaryl OCC was covalently functionalized to the purified (6,5)-SWCNTs via diazonium chemistry. *N*,*N*-Diethyl-4-animobenzene tetrafluoroborate was freshly synthesized from *N*,*N*-diethyl-*p*-phenylenediamine (97%, Sigma-Aldrich) and nitrous acid following a modified literature method[58]. The purified SWCNT solution was diluted with 1% sodium dodecylsulfate (≥99.0%, Sigma-Aldrich) and mixed with the synthesized diazonium salts to the carbon of (6,5)-SWCNT at a molar ratio of 3.17:1. The SWCNT–diazonium mixture was illuminated with a mercury arc lamp (X-Cite 120Q, Excelitas) at room temperature. After 20 min of illumination, the diazonium reaction was quenched by diluting the SWCNT solution with 1.04% DOC solution. The functionalized SWCNT solution was ultrafiltrated using Amicon Ultrafilters (100-kDa molecular weight cut-off).

DNA/DOC exchange for the OCC-functionalized SWCNTs

To redisperse the OCC–SWCNTs to biocompatible polymers, we partially adapted the literature method by Streit et al.[59]. First, we sequentially added 25 µl of 25 w:v% polyacrylamide (10 kDa; Sigma-Aldrich), 30 µl of ssDNA, 10 mg ml^{-1} (sequence = 5′-GTGTGTGTGTGT GTGTGTGTGTGTGTGTGT-3′ or 5′//Cy5/GTGTGTGTGTGTGTGTGTGT-GTGTGTGTGT//3′; Integrated DNA Technologies), 270 µl of methanol (anhydrous, 99.8%; Sigma-Aldrich) and 600 µl of 2-propanol (99.9%; Sigma-Aldrich) to the OCC–SWCNT solution. To precipitate DNA/polyacrylamide-encapsulated OCC–SWCNTs, the solution was centrifuged at 17,000g for 2 s. The supernatant was further centrifuged for 2 min at the same speed and room temperature. The pellets from each centrifugation were combined and redispersed with 150 µl of water. The addition of 600 µl of 2-propanol and centrifugation were repeated once more. The OCC–SWCNT pellets were then diluted in 1 ml of DNA, 4 mg ml^{-1}, PBS and tip sonicated for 1 h at 6 W and 4 °C. The solutions were ultracentrifuged at 100,000g and 4 °C for 30 min. Then, 85% of the supernatant was collected and dialyzed against PBS to remove free DNA (Spectra-Por, Float-A-Lyzer; molecular mass cut-off = 1 MDa). The absorption spectra of the OCC–DNA complexes were obtained using an ultraviolet visible-NIR spectrophotometer (V-780, Jasco). The absorbance at (6,5)E_{11} was used to estimate the relative OCC–DNA concentration[60].

NIR hyperspectral fluorescence microscopy

A hyperspectral microscope (IMA, Photon etc.) was used to obtain spectrally and spatially resolved OCC–DNA emission in live cells. A continuous-wave 808-nm laser (2 W) was injected into a multimode fiber to excite the nanosensors. The excitation beam passed through a beam-shaping module to produce a top-hat intensity profile with <10% power variation on the imaged region of the sample. The power output at the sample stage was 425.8, 370.2 and 164.8 mW for ×20, ×50 and ×100 objectives, respectively. A long-pass dichroic mirror with a cut-on wavelength of 875 nm (Semrock) was aligned to reflect the laser to the sample stage of an IX-71 inverted microscope equipped with LCPLN20XIR, LCPLN50XIR and LCPLN100XIR IR objectives (Olympus). Hyperspectral microscopy was conducted by passing the emission through a volume Bragg grating placed immediately before a thermoelectrically cooled, two-dimensional InGaAs detector (ZephIR 1.7) in the optical path.

Analysis and processing of hyperspectral data

Hyperspectral data acquired were saved as a (512 × 640 × 76) 16-bit array, where the first two coordinates signify the spatial location of a pixel and the last coordinate is its position in wavelength space, ranging from 950 nm to 1,250 nm with a 4-nm interval. Customized codes, written using MATLAB software, were used to subtract the background, correct for nonuniformities in excitation profile and wavelength-dependent quantum efficiency by each pixel, and compensate for dead pixels on the detector. A peak-finding algorithm was used to calculate the center wavelengths and intensities of the E_{11} and E_{11}^- peaks for a given pixel. To reduce the spectral drift resulting from the movement of lysosomes during the hyperspectral cube acquisition, 8 × 8 pixels were combined into a single pixel and the spectral parameters were obtained from the averaged emission spectrum. Pixels that failed the peak-finding threshold, primarily due to low intensity above the background, were removed from the datasets. The remaining pixels were fit with a Lorentzian function.

NIR fluorescence spectroscopy of OCC–DNAs

Fluorescence emission spectra of OCC–DNAs were acquired using a home-built NIR fluorescence spectroscopy. The SuperK EXTREME supercontinuum, white-light laser source (NKT Photonics) was used with a VARIA, variable bandpass filter accessory set to a bandwidth of 20 nm, centered at 575 nm. The light passed through a ×20 or ×50 NIR objective equipped in an inverted IX-71 microscope (Olympus) and illuminated the samples in a 96-well, clear flat-bottomed microplate (Corning). Emission from the OCC–DNAs was collected through the objective and passed through a dichroic mirror (875-nm cut-off, Semrock). A Shamrock 303i spectrograph (Andor, Oxford Instruments) with a slit width of 100 µm dispersed the emission using 86 g per mm of grating with a 1.35-µm blaze wavelength. The spectral range was 723–1,694 nm with a resolution of 1.89 nm. The light was collected by an iDus 1.7-µm InGaAs (Andor, Oxford Instruments) with an exposure time of 0.1–15 s. Background subtraction was conducted using a well in a 96-well plate filled with PBS or 10% FBS, depending on the experiment. After acquisition, the data were processed with customized codes written in MATLAB that applied the spectral corrections and background subtraction and fitted the emission peaks with Lorentzian functions.

OCC–DNA treatment in live cells for NIR fluorescence measurement

The nanosensors were added at 4–12 ng ml^{-1} to cell culture medium and incubated with cells at 30–60% confluency (8+ h) at 37 °C. These sensor treatment conditions were chosen because they resulted in a strong sensor signal with an exposure time of <15 s from all the tested cell lines with high biocompatibility. Then, 4 h after replacing with fresh medium, cells were trypsinized (Gibco) and replated on a 96-well microplate (Corning) or 35-mm glass-bottomed Petri dishes (MatTek). To compare uptake of OCC–DNAs in cells at different temperatures (4 and 37 °C), SKOV3 cells at 30% confluency in a 35-mm glass-bottomed dish were incubated in complete medium containing 0.1 mg l^{-1} of OCC–DNAs for 30 min. The cells were washed to remove cell surface-adsorbed OCC–DNA complexes and then incubated for 6 h in the OCC–DNA-free medium before fluorescence imaging. The fluorescence measurements were performed in a humidified chamber at 37 °C and 5% CO_2.

In vivo hyperspectral fluorescence spectroscopy

In vivo fluorescence imaging of the nanosensors was performed using a preclinical NIR hyperspectral mouse imaging system (IR VIVO, Photon and so on). We used 808-nm lasers to reduce tissue absorption and scattering of the excitation light in vivo. Excitation was provided by two continuous-wave diode lasers each with an output power of 2 W. Excitation light was distributed over the entire mouse with a maximum power density of 340 mW cm^{-2}. For hyperspectral animal imaging, the emission light was passed through a volume Bragg grating as described under NIR hyperspectral fluorescence microscopy. The E_{11} and E_{11}^{-} hyperspectral cubes were scanned for 950–1050 nm with a 10-nm step size and 1,100–1,200 nm with a 4-nm step size, respectively.

The pH calibration curves for live cells

The buffers for generating the pH calibration curves were formulated with 125 mM KCl, 25 mM NaCl, 10 μM monensin (≥97%; Sigma-Aldrich) and 25 mM Hepes (Sigma-Aldrich) for pH ≥ 7 buffers or 25 mM MES (Thermo Fisher Scientific) for pH < 7 buffers. Each buffer solution was adjusted to the appropriate final pH using 1 M NaOH or 1 M HCl. Cells treated with OCC–DNAs overnight were washed with fresh medium. Then 4 h after the medium exchange, the cells were washed with calibration buffer solutions 3×. The cells in buffer solution were plated in a 96-well plate at the cell density of approximately 0.3–0.6 × 10^6 cells per well. The OCC–DNA fluorescence emissions from the live cells were collected using an NIR fluorescence microscopy as described above.

Cell culture reagents and conditions

HEK293T, SKOV3, OVCAR3, HeLa and MEF cells were purchased from American Type Culture Collection. RM1 and Myc-CaP were gifts from the R. Blasberg lab (Memorial Sloan Kettering Cancer Center). All cells were grown at 37 °C in a 5% CO_2 incubator. HEK293T, SKOV3, HeLa, RM1, Myc-CaP and MEF cells were grown in Dulbecco's modified Eagle's medium (Gibco) with 10% FBS (Gibco); SKOV3 was supplemented with 100 μg ml^{-1} of primocin (InvivoGen), and RM1 and Myc-CaP were supplemented with 1× penicillin–streptomycin. OVCAR3 cells were grown in RPMI-1640 medium with 20% FBS supplemented with 100 μg ml^{-1} of primocin.

Cell viability assay

The cell viability assay was performed using the CellTiter-Glo 2.0 Assay (Promega). Cells were plated (2,000 cells per well) in 96-well plates (Corning) and treated with medium containing a concentration gradient of the OCC–DNAs (0.08–0.313 ng ml^{-1}) or PBS as a solvent control in triplicate (a 100-μl final volume of medium). After 72 h, the viability was quantified using intracellular ATP levels and 15 μl of CellTiter-Glo substrate was added into the cell medium and incubated for 40 min at room temperature. Luminescence was measured using a microplate reader (TECAN infinite M1000Pro) with 100-ms count time per well. For data processing, the luminescence value of PBS-treated cells was converted to 100% for each cell line and pH sensor-treated cells were normalized to the control as the relative viability.

NLRP3 inflammasomes and LDH cytotoxicity assay

Raw 264.7 cells stably expressing apoptosis-associated, speck-like protein containing a carboxy-terminal caspase recruitment domain (ASC) (Raw 264.7 cells do not endogenously express ASC) were treated with lipopolysaccharide (Invivogen, tlrl-3pelps) at 5 μg ml^{-1} for 16 h. The cells were treated with imiquimod (100 μM; Thermo Fisher Scientific, catalog no. 107471G), MCC950 (10 μM; Thermo Fisher Scientific, catalog no. NC1363755), or OCC–DNA complexes (0.1 mg ml^{-1}) alone or in combination with an NLRP3 inhibitor, MCC950 (10 μM), for 3 h. Supernatants were analyzed for lactate dehydrogenase (LDH) activity using the Pierce LDH Cytotoxicity Assay Kit (Life Technologies, catalog no. PI88953). LDH activity was quantified relative to a lysis control in which cells were lysed by adding 8 μl of a 9% Triton X-100 solution. Cells were collected for western blotting. Cell death was analyzed by LDH assay and western blotting for poly(ADP-ribose) polymerase (PARP) and GSDMD cleavage, an apoptosis marker and pyroptosis marker, respectively.

DQ-BSA assay

Cells, 100,000 cells per well, were plated in clear, flat-bottomed, CellBIND 48-well plates (Corning) and cultured until the cells reached 50–75% confluency. Cell medium was replaced with 200 μl of 800 nM calcein AM (Invitrogen) in Live cell imaging solution (Molecular Probes) for each well. An hour later, calcein AM-containing medium was removed and 200 μl of DQ-BSA, Red (Invitrogen), 25 μg ml^{-1}, in complete medium with 1 μg ml^{-1} of Hoechst stain was added to each well. A negative control group was added with Hoechst stain in complete medium only. After 1-h incubation, the medium was replaced by 200 μl of complete medium for each well and $t = 0$ h imaging of Cytation 5 was performed using Cell Imaging Multi-Mode Reader (BioTek). Then 200 μl of complete medium with a 2× concentration of the treatment of interest was added to the appropriate wells, and imaging reads were performed for every hour on Cytation 5. At least six fields of view between 100 and 1,000 cells were acquired in each well, with each treatment performed in two technical replicate wells. At least three independent biological experiments were performed for each cell line.

Antibodies and western blotting

Antibodies to LC3B (catalog no. NB100-2220), ATP6V1A (catalog no. NBP2-55148) and ATG7 (catalog no. NBP2-67596) were from Novus Biologicals. Antibodies to PARP (catalog no. 9542), glyceraldehyde 3-phosphate dehydrogenase (GAPDH, catalog no. 14C10), p70 S6 kinase (catalog no. 2708), phospho-p70 S6 kinase–Thr389 (catalog no. 9234), SQSTM1/p62 (catalog no. 39749) and β-actin (catalog no. 8457) were from Cell Signaling Technology. Mouse GSDMD rabbit monoclonal antibody (catalog no. ab209845) was from Abcam. IRDye 800CW goat anti-rabbit immunoglobulin G was from LI-COR Biosciences. After treatment, cells were lysed in Pierce RIPA buffer (Thermo Fisher Scientific) containing Halt protease and phosphatase inhibitor cocktails (Thermo Fisher Scientific). Cell lysate was normalized using Quick Start Bradford Dye Reagent (BioRad), prepared by adding 4× protein loading buffer (LI-COR Biosciences), heated at 98 °C for 5 min, resolved by 4–20% Mini-PROTEAN TGX Precast Polyacrylamide Gels (BioRad), western blotted and visualized using the Odyssey Imaging System (LI-COR Biosciences).

Colocalization study

SKOV3 cells were incubated with nanosensors (20 ng ml^{-1}) overnight. The cells were then washed 3× with PBS and placed in fresh cell medium. After 4 h, the cells were incubated with 5–50 nM LysoTracker Green DND-26 (Life Technologies) for 30 min in cell medium, washed 3× with PBS and imaged immediately in fresh PBS. For confocal fluorescence imaging of live cells, the FITC and Cy5 channels were used for LysoTracker Green and pH sensor, respectively. Cell imaging was performed on a Zeiss LSM 880, AxioObserver microscope equipped with a Plan-Apochromat ×63 oil 1.4 numerical aperture (NA) differential interference contrast M27 objective in a humidified chamber at 37 °C and 5% CO_2. For colocalizing nanosensor emission and LysoTracker Green, after the PBS wash, the cells were placed in fresh medium with DMSO, 100 μM of EN6, 250 nM of torin 1 or 100 nM of Baf A1. The LysoTracker Green emission was collected using an EMCCD camera with an FITC channel and the broadband emission of pH sensor was collected using a two-dimensional InGaAs camera of a NIR fluorescence microscopy as described above. The measurements were performed in a humidified chamber at 37 °C and 5% CO_2. After the fluorescence microscopy measurements, the images were processed for colocalization analysis in ImageJ with split channels of Cy5 (or nanosensors) and LysoTracker Green. The JACoP plugin[61] was used to obtain Manders' coefficients.

The colocalization analysis of the tumor tissue immunofluorescence images was performed on Cy5-ss$(GT)_{15}$-wrapped, pH sensor-injected SKOV3 tumors. Serial tissue sections, 5 μm, were used for analysis. The fluorescent tissue images of Cy5-labeled CNTs were stained with DAPI, and the serial tissue sections were stained with DAPI and LAMP1. The slides were scanned with a ×20/0.8 NA objective on a Pannoramic Confocal Scanner (3DHistech). DAPI images were used to superimpose two consecutive images using a customized

MATLAB code. The superimposed images of DAPI, Cy5 and LAMP1 were processed for colocalization analysis using the JACoP plugin[61] implemented in ImageJ.

AFM

A stock solution of nanosensors at 7 mg l^{-1} in 1× PBS was diluted 20× in deuterated (d)H_2O and plated on a freshly cleaved mica substrate (SPI) for 4 min before washing with 10 ml of water and blowing dry with argon gas. An Olympus AC240TS AFM probe (Asylum Research) in an Asylum Research MFP-3D-Bio instrument was used to image in AC mode. Data were captured at 2.93-nm per pixel *xy* resolution and 15.63-pm *z*-resolution.

Animal studies

All animal studies were approved by and carried out in accordance with the Memorial Sloan Kettering Cancer Center Institutional Animal Care and Use Committee. Female Hsd:Athymic Nude-Foxn1nu mice were purchased from Envigo at age 5–6 weeks. All control and experimental mice were age matched and housed in air-filtered laminar flow cabinets with freely available food and water under a 12-h light:dark cycle, 18–23 °C and 40–60% humidity. Approximately 1 million SKOV3 tumor cells were injected subcutaneously in a 1:1 mixture of serum-free medium and Matrigel (BD Biosciences) into both flanks (200 µl per flank). When the tumor volume reached 100 mm^3, mice were randomized and 30 ml of the nanosensors (0.1 mg l^{-1}, diluted in PBS) or PBS (control) was intratumorally injected in one flank, After 24 h, the mice were intraperitoneally injected with EN6 (50 mg kg^{-1}), Baf A1 (0.125 mg kg^{-1}), torin 1 (20 mg kg^{-1}) or vehicle (saline:DMSO:PEG 400, v:v:v = 6:1:1). For in vivo imaging and spectroscopy, mice were anesthetized with 2% isoflurane before and during data collection. Animals were euthanized using CO_2 inhalation. Tumors were harvested for histology analysis.

Immunohistochemistry and immunofluorescence

The immunohistochemical imaging was performed at the Weill Cornell Medicine, Department of Pathology and Laboratory Medicine, Center for Translational Pathology, and Memorial Sloan Kettering Cancer Center Molecular Cytology Core Facility. At the experimental endpoint, subcutaneously engrafted tumor tissue was retrieved and fixed in 10% formalin at 4 °C for 24 h and embedded in paraffin after dehydration. Sections, 5 µm, were used for analysis.

The immunohistochemistry for p62/SQSTM1 (Enzo Life Science, catalog no. BML-PW9860-0025; Antigen retrieval BOND Epitope Retrieval Solution 2, catalog no. AR9640-ER2, pH 9 for 20 min, antibody dilution 1:100 with 15-min incubation time at room temperature) was developed on Leica Bond Rx with a default protocol by Pathology Core at Weill Cornell Medical Center.

The immunohistochemical detection for pS6K and the immunofluorescence detection of LAMP1 were performed using Discovery XT processor or Ultra processor (Ventana Medical Systems-Roche). The tissue sections for pS6K were deparaffinized with EZPrep buffer (Ventana Medical Systems), antigen retrieval was performed with CC1 buffer (Ventana Medical Systems-Roche) and sections were blocked for 30 min with background buster solution (Innovex). A rabbit monoclonal anti-PS6R (Cell Signaling) was used in 0.36 mg ml^{-1} concentration. The incubation with the primary antibody was done for 6 h, followed by 1-h incubation with biotinylated goat anti-rabbit immunoglobulin G (VectorLabs) in 5.75 mg ml^{-1}. Blocker D, streptavidin–horseradish peroxidase (HRP) and DAB detection kit (Ventana Medical Systems) were used according to the manufacturer's instructions. The slides were counterstained with hematoxylin and coverslipped with Permount (Thermo Fisher Scientific). Image quantification of p62/SQSTM1 and pS6K staining and nuclei count were taken using Qupath 0.2 (ref. 62).

For the LAMP1 staining, after 32 min of heat and standard retrieval via cell conditioning 1 (Ventana), the tissue sections were blocked first for 30 min in background blocking reagent (Innovex). A rabbit monoclonal LAMP1 (Cell Signaling) was used at 0.34 µg ml^{-1}. Primary antibody was incubated for 5 h, followed by incubation with biotinylated goat anti-rabbit IgG (VectorLabs) at 5.75 mg ml^{-1} for 1 h. Blocker D, streptavidin–HRP and tyramide-CF594 (Biotium) were prepared and applied according to manufacturer's instruction in 1:2,000 for 16 min. All slides were counterstained in 5 µg ml^{-1} of DAPI (Sigma-Aldrich, catalog no. D9542), for 5 min at room temperature, mounted with anti-fade mounting medium Mowiol 4-88 (Millipore) and coverslipped.

Statistics and reproducibility

Statistical analysis was performed with GraphPad Prism v.8.4.3. All data met the assumptions of the statistical tests performed (that is, normality, equal variances). Statistical parameters and significance are reported in the figures or figure legends. Sample size decisions were based on the instrumental signal:noise ratios. AFM, hyperspectral and confocal microscopy images were repeated at least 5× with comparable results. Immunohistochemistry and immunofluorescence staining were performed on all mice used in the studies ($n = 5$ biological replicates per group). All cellular experiments and western blotting were performed at least 3× with comparable results.

Ethics statement

All animal procedures used in the present study were performed in accordance with the protocol approved by the Memorial Sloan Kettering Cancer Center Institutional Animal Care and Use Committee.

Reporting summary

Further information on research design is available in the Nature Portfolio Reporting Summary linked to this article.

Data availability

Source data are provided with this paper.

Code availability

LABVIEW code for data acquisition and MATLAB codes for data analysis in this article are available in the public GitHub repository (github.com/mijinee/HellerLab_MSKCC).

References

57. Subbaiyan, N. K. et al. Role of surfactants and salt in aqueous two-phase separation of carbon nanotubes toward simple chirality isolation. *ACS Nano* **8**, 1619–1628 (2014).
58. Quintero, B., Cabeza, M. C., Martínez, M. I., Gutiérrez, P. & Martínez, P. J. Dediazoniation of *p*-hydroxy and *p*-nitrobenzenediazonium ions in an aqueous medium: interference by the chelating agent diethylenetriaminepentaacetic acid. *Can. J. Chem.* **81**, 832–839 (2003).
59. Streit, J. K., Fagan, J. A. & Zheng, M. A low energy route to DNA-wrapped carbon nanotubes via replacement of bile salt surfactants. *Anal. Chem.* **89**, 10496–10503 (2017).
60. Zheng, M. & Diner, B. A. Solution redox chemistry of carbon nanotubes. *J. Am. Chem. Soc.* **126**, 15490–15494 (2004).
61. Bolte, S. & CordeliÈRes, F. P. A guided tour into subcellular colocalization analysis in light microscopy. *J. Microsc.* **224**, 213–232 (2006).
62. Bankhead, P. et al. QuPath: open source software for digital pathology image analysis. *Sci. Rep.* **7**, 16878 (2017).

Acknowledgements

We thank Memorial Sloan Kettering Cancer Center (MSKCC) Molecular Cytology Core Facility for assistance with AFM imaging, sample processing for immunofluorescence and confocal microscopy, and image analysis. We also thank the Center for Translational Pathology at Weill Cornell Medicine for immunohistochemistry.

We thank C. O'Mara at the Daniel Bachovchin lab (MSKCC) for the NLRP3 inflammasome experiment. We thank P. Jena for assistance with image processing and analysis. The graphical abstract, Fig. 3a and Supplementary Figs. 2 and 11 were created with BioRender.com. This work was supported in part by the National Science Foundation CAREER Award (grant no. 1752506 to D.A.H.), the National Cancer Institute (grant no. R01-CA215719 to D.A.H. and Cancer Center Support grant no. P30-CA008748 to D.A.H., H.A. and Y.M.L.), the National Institutes of Health (NIH) Common Fund (grant no. DP2-HD075698 to D.A.H.), the Department of Defense Congressionally Directed Medical Research Program (W81XWH2210563 to D.A.H.), the American Cancer Society Research Scholar grant (no. GC230452 to D.A.H.), the Ara Parseghian Medical Research Fund (to D.A.H.), the Honorable Tina Brozman Foundation (to D.A.H.), the Ovarian Cancer Research Alliance and the Edmée Firth Fund for Research in Ovarian Cancer (grant no. CRDGAI-2023-3-1003 to D.A.H.), the Pershing Square Sohn Cancer Research Alliance (to D.A.H.), the New York State Biodefense Commercialization Fund (to D.A.H.), the Expect Miracles Foundation—Financial Services Against Cancer (to D.A.H.), the Louis and Rachel Rudin Foundation (to D.A.H.), the Experimental Therapeutics Center of MSKCC (to D.A.H. and Y.M.L.), Mr. William H. Goodwin and Mrs. Alice Goodwin and the Commonwealth Foundation for Cancer Research (to D.A.H. and Y.M.L.), the JPB Foundation (to Y.M.L.) and the William Randolph Hearst Fund in Experimental Therapeutics (to Y.M.L.). M.K. was supported by the NIH (grant no. K99-EB033580) and the Marie-Josée Kravis Women in Science Endeavor Postdoctoral Fellowship. Z.Y. was supported by the Ann Schreiber Mentored Investigator Award (Ovarian Cancer Research Fund) and Young Investigator 2019 (Kaleidoscope of Hope). R.L. was supported by an NIH T32 training grant (no. T32-GM73546), J.W. was supported by an NIH T32 training grant (no. T32-GM136640-Tan). D.W. was supported by NIH T32 training grants (nos. T32-GM141949 and T32-CA062948). R.F. was supported by the Alfred Benzon Foundation Fellowship. Y.H.W. acknowledges support from the National Science Foundation (grant nos. CHE-1904488 and CHE-2204202).

Author contributions

M.K., C. Chen, R.F., D.A.H., H.A. and Y.H.W. conceived the idea. M.K., C. Chen, R.F. and D.A.H. designed experiments. M.K., C. Chen, and D.A.H. analyzed the data. M.K., E.R. and X.W. performed nanosensor synthesis. M.K., C. Chen, R.F., E.R., J.W., C. Cupo, R.E.L., D.W.W., R.L. and D.G. performed in vitro experiments. M.K., C. Chen, Z.Y. and J.S. performed in vivo experiments. M.K., C. Chen and D.A.H. wrote the manuscript. Y.M.L., H.A. and Y.H.W. edited the manuscript.

Competing interests

D.A.H. is a cofounder and officer with equity interest in Lime Therapeutics, Inc., cofounder with equity interest in Selectin Therapeutics Inc. and Resident Diagnostics, Inc., and a member of the scientific advisory board of Concarlo Therapeutics, Inc., Nanorobotics Inc. and Mediphage Bioceuticals, Inc. The remaining authors declare no competing interests.

Additional information

Extended data is available for this paper at https://doi.org/10.1038/s41589-023-01364-9.

Supplementary information The online version contains supplementary material available at https://doi.org/10.1038/s41589-023-01364-9.

Correspondence and requests for materials should be addressed to Daniel A. Heller.

Peer review information *Nature Chemical Biology* thanks Jiajie Diao and the other, anonymous, reviewer(s) for their contribution to the peer review of this work.

https://doi.org/10.1038/s41589-023-01364-9

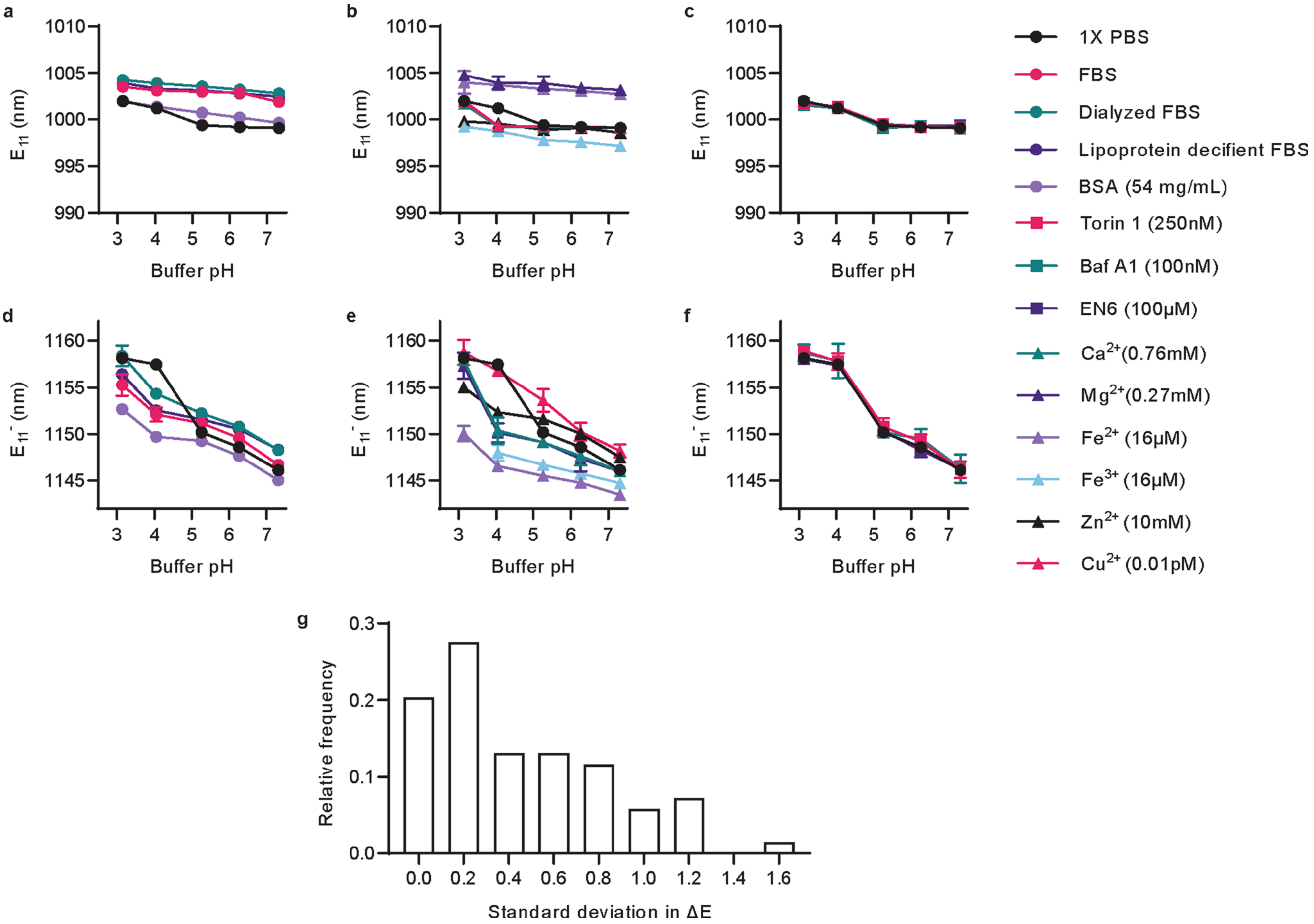

Extended Data Fig. 1 | Characterization of OCC-DNA response in various buffer/media conditions. Emission wavelengths of **a**-**c**, E_{11} and **d**-**f**, E_{11}' of the OCC-DNA complexes at varying buffer pH and media conditions in phosphate buffered saline. The metal ion concentrations tested are physiologically relevant ranges. All data are presented as mean values and error bars denote standard deviation from N = 3 technical replicates (**a**-**f**). **g**, Frequency distribution of standard deviations of ΔE (= $E_{11}' - E_{11}$) wavelength shifts of triplicate measurements of **a**-**f**.

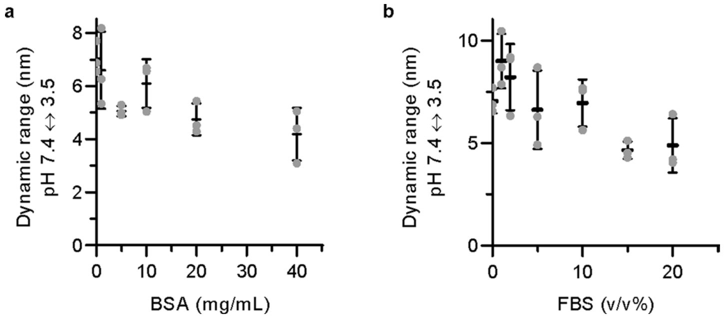

Extended Data Fig. 2 | Protein concentration effects on OCC-DNA optical response. The dynamic range of the OCC-DNA response to pH at increasing concentrations of: **a**, bovine serum albumin and **b**, fetal bovine serum. All data are presented as mean values and error bars denote standard deviation from N = 3 technical replicates (**a**,**b**).

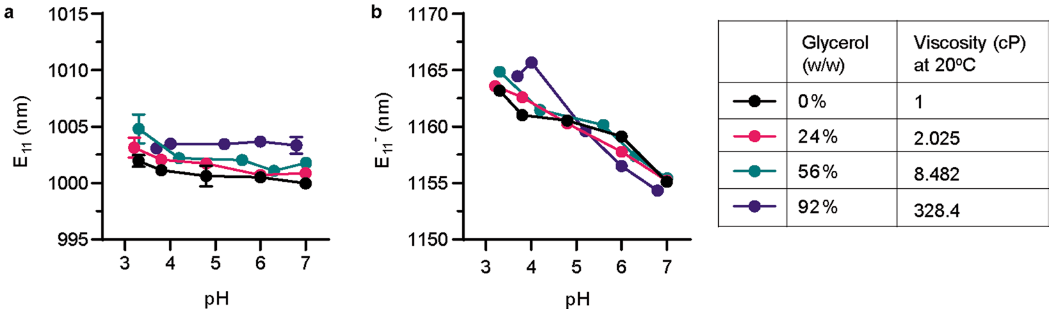

	Glycerol (w/w)	Viscosity (cP) at 20°C
●	0%	1
●	24%	2.025
●	56%	8.482
●	92%	328.4

Extended Data Fig. 3 | Viscosity effects on OCC-DNA optical response. Emission wavelengths of **a**, E_{11} and **b**, E_{11}^{-} of the OCC-DNA complexes at varying buffer pH and glycerol. All data are presented as mean values and error bars denote standard deviation from N = 3 technical replicates (**a**,**b**).

https://doi.org/10.1038/s41589-023-01364-9

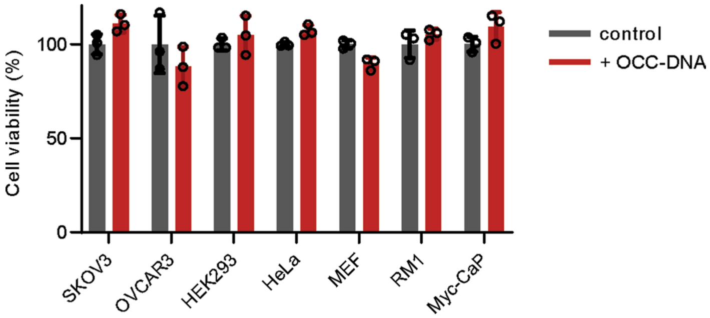

Extended Data Fig. 4 | Cell viability in response to OCC-DNA complexes. Single-dose (0.01 mg/L) OCC-DNA cell viability of SKOV3, OVCAR3, HEK293, HeLa, MEF, RM1, and Myc-CaP cell lines, measured via CellTiter-Glo 2.0, after 72 hours of incubation. No statistically significant differences were observed between the PBS control groups (gray) and the treatment groups (red) in all the tested cell lines. All data are presented as mean values and error bars denote standard deviation of triplicates for each condition.

https://doi.org/10.1038/s41589-023-01364-9

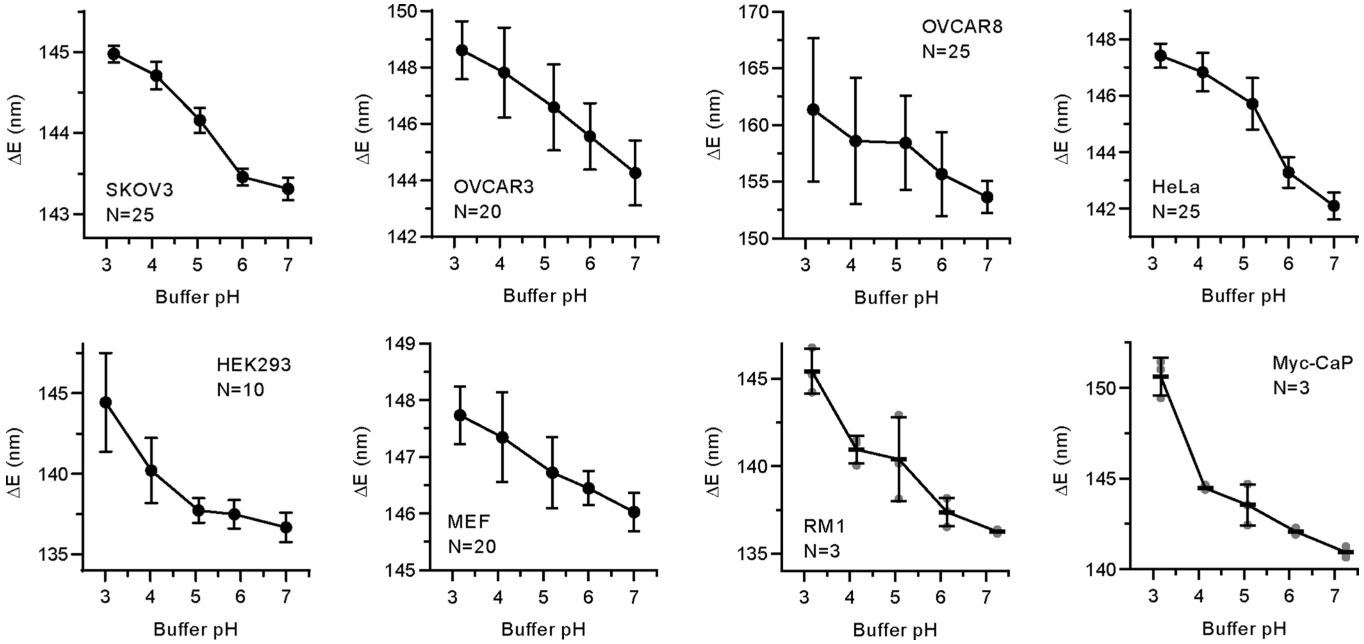

Extended Data Fig. 5 | OCC-DNA responses in 8 cell lines. The emission response ($\Delta E = E_{11}^{-} - E_{11}$) of OCC-DNAs in live cells upon exposure to HEPES or MES buffer solutions of varying pHs with monensin (see Methods). All data are presented as mean values and error bars denote standard deviation from N = 3–25 biological replicates.

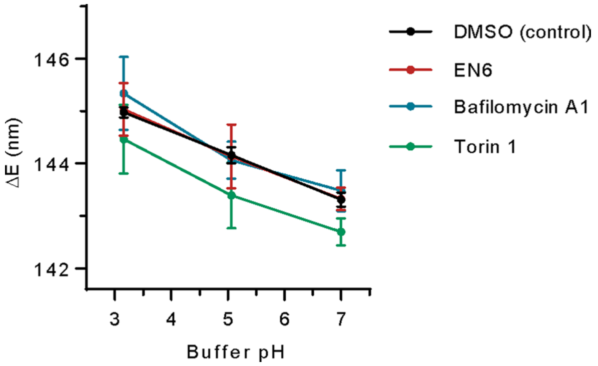

Extended Data Fig. 6 | Inhibitor-mediated alterations of nanosensor response to pH. The emission response ($\Delta E = E_{11}^{-} - E_{11}$) of nanosensors in live SKOV3 cells upon exposure to HEPES or MES buffer solutions of varying pHs with monensin (see Methods). Cells were treated with DMSO (black), 100 µM EN6 (red), 100 nM bafilomycin A1 (blue), 250 nM torin 1 (green) for 4 hours prior to pH measurements. Data are presented as mean values and error bars denote standard deviation from N = 25 each DMSO, EN6, and Baf A1 point, and N = 25, 24, and 21 for pH 7, 5.06, and 3.16 for torin 1 as biological replicates.

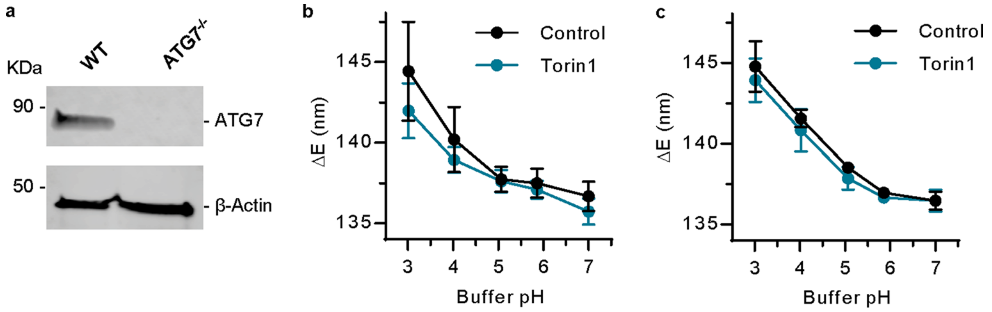

Extended Data Fig. 7 | Nanosensor response in autophagy-defective cells. **a**, ATG7 expression by western blotting confirmed the knockout of ATG7 in the HEK293T cell line used herein. The emission wavelength response ($\Delta E = E_{11}^{-} - E_{11}$) of OCC-DNAs in live **b**, wild type and **c**, ATG7$^{-/-}$ HEK293T cells upon exposure to HEPES or MES buffer solutions of varying pHs in the presence of monensin (see Methods). Cells were treated with DMSO (black) or 250 nM torin 1 (blue) for 4 hours prior to pH measurements. All data are presented as mean values and error bars denote standard deviation from N = 10 technical replicates (**b**,**c**). Original gel images are in Supplementary Fig. 24.

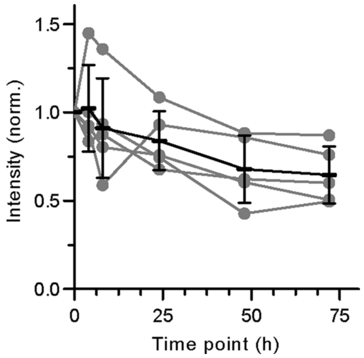

Extended Data Fig. 8 | Time-dependent fluorescence intensity changes of intratumorally-injected nanosensors. Quantification of total emission intensity of nanosensors in solid tumours of mice after injection. Fluorescence measurements were performed with a near-infrared preclinical hyperspectral imager with 730 nm excitation. Data are presented as mean values and error bars denote standard deviation from N = 5 biological replicates.

nature portfolio

Corresponding author(s): Daniel Heller

Last updated by author(s): Apr 17, 2023

Reporting Summary

Nature Portfolio wishes to improve the reproducibility of the work that we publish. This form provides structure for consistency and transparency in reporting. For further information on Nature Portfolio policies, see our Editorial Policies and the Editorial Policy Checklist.

Statistics

For all statistical analyses, confirm that the following items are present in the figure legend, table legend, main text, or Methods section.

n/a	Confirmed	
☐	☒	The exact sample size (*n*) for each experimental group/condition, given as a discrete number and unit of measurement
☐	☒	A statement on whether measurements were taken from distinct samples or whether the same sample was measured repeatedly
☐	☒	The statistical test(s) used AND whether they are one- or two-sided *Only common tests should be described solely by name; describe more complex techniques in the Methods section.*
☒	☐	A description of all covariates tested
☐	☒	A description of any assumptions or corrections, such as tests of normality and adjustment for multiple comparisons
☐	☒	A full description of the statistical parameters including central tendency (e.g. means) or other basic estimates (e.g. regression coefficient) AND variation (e.g. standard deviation) or associated estimates of uncertainty (e.g. confidence intervals)
☐	☒	For null hypothesis testing, the test statistic (e.g. *F*, *t*, *r*) with confidence intervals, effect sizes, degrees of freedom and *P* value noted *Give P values as exact values whenever suitable.*
☒	☐	For Bayesian analysis, information on the choice of priors and Markov chain Monte Carlo settings
☒	☐	For hierarchical and complex designs, identification of the appropriate level for tests and full reporting of outcomes
☒	☐	Estimates of effect sizes (e.g. Cohen's *d*, Pearson's *r*), indicating how they were calculated

Our web collection on statistics for biologists contains articles on many of the points above.

Software and code

Policy information about availability of computer code

Data collection	Custom LABVIEW codes were used for automated fluorescence spectroscopy, available in github.com/mijinee/HellerLab_MSKCC PhySpec software version 2.25.6 was used to obtain hyperspectral near-infrared fluorescence images.
Data analysis	Custom MATLAB codes were used for background subtraction, spectral corrections, and peak fitting of fluorescence spectra. We provide the codes for data processing in github.com/mijinee/HellerLab_MSKCC The statistical analyses were performed with GraphPad Prism version 9.3.0. The colocalization image analysis was performed using the JACoP plugin implemented in ImageJ version 2.35

For manuscripts utilizing custom algorithms or software that are central to the research but not yet described in published literature, software must be made available to editors and reviewers. We strongly encourage code deposition in a community repository (e.g. GitHub). See the Nature Portfolio guidelines for submitting code & software for further information.

Data

Policy information about availability of data

All manuscripts must include a data availability statement. This statement should provide the following information, where applicable:

- Accession codes, unique identifiers, or web links for publicly available datasets
- A description of any restrictions on data availability
- For clinical datasets or third party data, please ensure that the statement adheres to our policy

All data is available in the manuscript or the supplementary materials.

Human research participants

Policy information about studies involving human research participants and Sex and Gender in Research.

Reporting on sex and gender	N/A
Population characteristics	N/A
Recruitment	N/A
Ethics oversight	N/A

Note that full information on the approval of the study protocol must also be provided in the manuscript.

Field-specific reporting

Please select the one below that is the best fit for your research. If you are not sure, read the appropriate sections before making your selection.

☒ Life sciences ☐ Behavioural & social sciences ☐ Ecological, evolutionary & environmental sciences

For a reference copy of the document with all sections, see nature.com/documents/nr-reporting-summary-flat.pdf

Life sciences study design

All studies must disclose on these points even when the disclosure is negative.

Sample size	Sample sizes were chosen based on recommendations from prior literature regarding number of samples for in vivo carbon nanotube research (e.g., Harvey et al., Nat Biomed Eng 2017, Williams et al, Sci Adv 2018) and for intrinsic variability in cell experiments (Chung et al Nat Chem Bio 2019), and our own expertise. For live cell fluorescence studies, replicates were chosen to ensure statistical power to account for cell-to-cell and measurement-tomeasurement variations and ensure repeatability. For animal studies, numbers were chosen based on statistical spread of the in vitro data and to minimize animal use
Data exclusions	No data were excluded from the analyses.
Replication	All experiments were performed in replicates and noted in main text, figures or methods. Fluorescence measurements on each sample were done with triplicate to confirm the consistency of the measurements, and at least repeated three times. All attempts at replication were successful.
Randomization	All samples were randomized and allocated into different groups. For in vivo experiments, after nanosensor injection into SKOV3 tumors, mice were randomized into four different treatment groups. For cell experiments, randomization was not performed. For example, immunoblotting samples required to collect and load in a specific order to generate the final results.
Blinding	Blinding was not applied in vitro experimentation. This was done for practical purposes and is standard for similar types of experiments. The quantitative results are not affected by blinding. For in vivo experiments, cages, sample collection, and data processing were labeled as code names that were only revealed and organized by the end. The investigators were not blinded to treatment groups for practical purposes.

Reporting for specific materials, systems and methods

We require information from authors about some types of materials, experimental systems and methods used in many studies. Here, indicate whether each material, system or method listed is relevant to your study. If you are not sure if a list item applies to your research, read the appropriate section before selecting a response.

Materials & experimental systems

n/a	Involved in the study
☐	☒ Antibodies
☐	☒ Eukaryotic cell lines
☒	☐ Palaeontology and archaeology
☐	☒ Animals and other organisms
☒	☐ Clinical data
☒	☐ Dual use research of concern

Methods

n/a	Involved in the study
☒	☐ ChIP-seq
☒	☐ Flow cytometry
☒	☐ MRI-based neuroimaging

Antibodies

Antibodies used	Primary antibodies: LC3B (NB100-2220), ATP6V1A (NBP2-55148), and ATG7 (NBP2-67596) were from Novus Biologicals. PARP (9542), GAPDH (14C10), p70 S6 Kinase (2708), phospho-p70 S6 Kinase – Thr389 (9234), SQSTM1/p62 (39749), LAMP1 (9091), phospho-S6 Ribosomal Protein - Ser235/236 (4858) and beta Actin (8457) were from Cell Signaling Technology. Mouse GSDMD rabbit monoclonal antibody (ab209845) was from Abcam. p62 (human) polyclonal antibody (BML-PW9860-0025) was from Enzo Life Sciences. Secondary antibodies: IRDye 800CW Goat anti-Rabbit IgG (926-32211) was from LI-COR Biosciences. Biotinylated Goat anti-Rabbit IgG was from Vector Laboratories (PK-6101).
Validation	All antibodies used were commercially available and have been validated by the manufactures accordingly. anti-LC3B: https://www.novusbio.com/products/lc3b-antibody_nb100-2220#datasheet anti-ATP6V1A: https://www.novusbio.com/products/atp6v1a-antibody_nbp2-55148#datasheet anti-ATG7: https://www.novusbio.com/products/atg7-antibody-sc06-30_nbp2-67596#datasheet anti-PARP: https://www.cellsignal.com/products/primary-antibodies/parp-antibody/9542 anti-GAPDH: https://www.cellsignal.com/products/primary-antibodies/gapdh-14c10-rabbit-mab/2118?site-search-type=Products&N=4294956287&Ntt=14c10&fromPage=plp anti-p70 S6 Kinase:https://www.cellsignal.com/products/primary-antibodies/p70-s6-kinase-49d7-rabbit-mab/2708 anti-phospho-p70 S6 Kinase – Thr389: https://www.cellsignal.com/products/primary-antibodies/phospho-p70-s6-kinase-thr389-108d2-rabbit-mab/9234 anti-SQSTM1/p62:https://www.cellsignal.com/products/primary-antibodies/sqstm1-p62-d1q5s-rabbit-mab/39749 anti-LAMP1: https://www.cellsignal.com/products/primary-antibodies/lamp1-d2d11-xp-rabbit-mab/9091 anti-phospho-S6 Ribosomal Protein - Ser235/236: https://www.cellsignal.com/products/primary-antibodies/phospho-s6-ribosomal-protein-ser235-236-d57-2-2e-xp-rabbit-mab/4858 anti-beta Actin: https://www.cellsignal.com/products/primary-antibodies/b-actin-d6a8-rabbit-mab/8457 anti-GSDMD:https://www.abcam.com/products/primary-antibodies/gsdmd-antibody-epr19828-ab209845.html anti-p62(human): https://www.enzolifesciences.com/BML-PW9860/p62-human-polyclonal-antibody/

Eukaryotic cell lines

Policy information about cell lines and Sex and Gender in Research

Cell line source(s)	HEK293T, SKOV3, OVCAR3, HeLa, MEF were purchased from ATCC. RM1 and Myc-CaP were gifted from the Ronald Blasberg Lab at Memorial Sloan Kettering Cancer Center. Raw 264.7 (expressing ASC) was provided by Daniel Bachovchin lab mat Memorial Sloan Kettering Cancer Center.
Authentication	HEK293T, SKOV3, OVCAR3, HeLa, MEF were not authenticated since they were directly purchased from ATCC. RM1 and Myc-CaP were authenticated by morphology. Raw 264.7 (expressing ASC) was authenticated by immunoblotting.
Mycoplasma contamination	All cell lines tested negative for mycoplasma contamination using MycoAlert Mycoplasma Detection Kit (Lonza, LT07-318)
Commonly misidentified lines (See ICLAC register)	No commonly misidentified lines were used

Animals and other research organisms

Policy information about studies involving animals; ARRIVE guidelines recommended for reporting animal research, and Sex and Gender in Research

Laboratory animals	Female Hsd:Athymic Nude-Foxn1nu mice (Envigo), 5-6 weeks old. All control and experimental mice were age-matched and housed in air-filtered laminar flow cabinets with food and water ad libitum. Animals were housed on a 12-hour (hr) light/dark cycle with standard mouse room temperatures between 18-23 C with 40-60% humidity per MSKCC RARC animal facility guidelines.
Wild animals	The study did not involve wild animals
Reporting on sex	Only female mice were used for the ovarian cancer cell line (SKOV3).
Field-collected samples	The study did not involve field-collected samples

Ethics oversight	All animal procedures used in this study were performed in accordance with the protocol approved by the Memorial Sloan Kettering Cancer Center Institutional Animal Care and Use Committee

Note that full information on the approval of the study protocol must also be provided in the manuscript.